The Design of Printed Hybrid Constructs to Serve as Cartilage Templates for Bone Repair

A Thesis

Submitted to the Faculty

of

Drexel University

by

Nathan Tessema Ersumo

in partial fulfillment of the

requirements for the degree

of

Master of Science

June

2017

Drexel
UNIVERSITY

Acknowledgements

I would like to acknowledge and thank my primary advisor, Dr. Kara Spiller, and the entirety of the Biomaterials & Regenerative Medicine Laboratory for helpful feedback, suggestions and guidance.

Special thanks to the Cell Imaging Center at Drexel University, Claire Witherel for work in with cell studies, as well as technical assistance from Ricardo Solorzano, Victoria Leon, Hannah Geisler, Austin Philip, Brandon Marcinkiewicz, Frank Kepics and Dolores Conover. I thank Dr. Sriram Balasubramanian for helpful discussions as well.

I would also like to acknowledge the entirety of Prof. Rui Reis' 3B's Research Group at the University of Minho in Portugal, where experiments for the second aim were completed. Specifically, I'd like to thank my advisor Dr. Vitor Correlo and assistance from Tírcia Santos, Sarah Oliveira and Pathomthat Srisuk.

Finally, special thanks to Dr. Lin Han and Dr. Adrien Shieh for joining my thesis committee and providing helpful feedback.

Table of Contents

List of Tables

List of Figures

dissolution of the sacrificial PEG network, leading to the formation of a secondary porous network.

12. Interplay between pore and hydrogel geometries alters the time-dependent mechanical properties of prepared constructs.

13. Hydrogels in 0P/1HG constructs and weight-matched plain hydrogel control exhibit different swelling behavior.

Abstract

With an estimated annual incidence of over 2.2 million cases across the world, critical size bone defects pose an unmet challenge requiring improved therapeutic strategies. Current clinical solutions, namely autologous and allogeneic grafts, are associated with a number of complications which include supply shortage, donor site morbidity and immune rejection. Given the poor vascularization observed with bioresorbable bone template scaffolds, some have turned to engineering the endogenous repair pathway by developing implantable cartilage templates susceptible to the bone transformation process known as endochondral ossification seen in native defects. Yet considerations relating to the implants' mechanical behavior, porosity and swelling, all of which are crucial to mimicking the endochondral ossification process, remain largely unaddressed in past studies. Through a parameter-driven preliminary study, we've devised a method to improve spatial resolution and property modulation by incorporating additive manufacturing into the fabrication process of cartilage templates destined for ossification-mediated defect repair. Based on our findings that hydrogel extrusion introduces structural discontinuities leading to excessive swelling and time-dependent mechanical deformation, we advance a biofabrication method involving (1) the 3D printing of a porous hybrid construct comprised of a stiff polycaprolactone network interwoven with sacrificial poly(ethylene glycol) material, (2) the casting of a cell-laden hydrogel material into the primary porous network and (3) the evacuation of the sacrificial poly(ethylene glycol) material to create a secondary porous network. The architecture of the generated templates was modulated by varying the widths of the secondary pores and hydrogel struts. Generated templates were subjected to geometric analysis by photography, porosity evaluation by micro-computed tomography, stress relaxation testing and a swelling study. The incorporation of a stiff network constrained swelling by more than half while decreased porosity-to-hydrogel content ratios mitigated time-dependent deformation.

1. Background

1.1. Bone defect injury and existing solutions

Though bone has an exceptional capacity for regeneration, repairing severe bone defects remains a critical challenge. Indeed, once defects surpass a critical size, native pathways are no longer able to regenerate the defect area, leading to the formation of non-union gaps which amount to 100,000 fracture cases each year in the US alone [1]. The most salient and grave examples of such non-union gaps occur in long bones, and more specifically across the mid-section (diaphysis or metaphysis) of long bones [2]. In such cases, gap lengths need only be 2.5 to 3 times the diameter of the affected long bone for self-healing to not occur [3], though smaller gaps may also lead to non-unions. In tibias, for instance, a 25 mm gap is sufficient to preclude regeneration without intervention [4]. Overall, over 2.2 million annual cases in the world primarily linked to traumatic injury require the use of bone grafting, generating an annual cost of $2.5 billion [5]. Moreover, despite the predominance of high-energy injuries in the occurrence of bone defects, a number of other conditions may also lead to the formation of non-unions gaps in bones. Indeed, osteosarcoma, the most common type of primary bone tumor which represents 1% of all cancers in the US, requires the resection of tumors, 85.5% of which occur in long bones, often leaving critical size bone gaps at excision sites [6]. In addition, bones may succumb to infection by bacteria from species including *Staphylococcus*, *Pseudomonas* and *Aspergillus* [7, 8]. Such infection leads to an inflammatory bone disorder known as osteomyelitis, characterized by bone necrosis and destruction, and occurring in long bones in approximately 55% of cases [9]. Whether due to trauma, cancer or infection, the negative impacts of bone defects reverberate from local responses, which include inflammation, widespread soft tissue damage and

compromised vascularity, to functional consequences such as loss of mobility due to severe instability and possible sepsis from infection [10].

Thus, almost invariably, massive bone defects require immediate surgical intervention in the form of excision/debridement followed by fixation through the use of compression plates, nails, wires or cement [11]. However, despite its necessity, fixation alone is not a viable treatment strategy since, in accordance with Wolff's law, the resulting mechanical unloading from immobilization leads to bone loss in regions adjacent to the defect site [12, 13]. Bridging critical size gaps to promote regeneration therefore constitutes a vital complement to temporary fixation in intervention strategies for non-union defects. Though autografts and allografts remain the gold standard in bone graft substitutes, they are associated with a number of complications, including donor site morbidity and supply shortage for autografts [14], immune rejection, infectious disease transmission and socio-religious refusal for allografts [5, 11]. Accordingly, a number of biomaterial-based strategies are being investigated in order to develop a graft capable of osseointegration and load bearing functionality while promoting regeneration.

Metal and ceramic implants, coupled with osseointegrative methods including surface functionalization/coating [15] and therapeutic release [16], constitute one area of investigation. However, the non-degradable nature of these implants precludes the possibility for full repair through resorption and regeneration. Another active area of investigation has therefore been the development of bioresorbable polymer scaffolds as potential grafts. This strategy aims to induce the transition from implanted scaffold to newly generated bone tissue through the encapsulation of cells, such as mesenchymal stem cells (MSCs) [17], or the incorporation of immunomodulatory drugs [18] and proteins such as bone morphogenetic proteins (BMPs) [19]. Such approaches are governed by spatiotemporal requirements pertaining to the biomechanical

properties of the scaffolds. Indeed, upon implantation, the scaffolds must first match the physical demands of the surrounding bone to withstand native loads without contributing to stress shielding [20, 21]. Subsequently, the structure and fixation positioning of the scaffolds must trigger adequate mechanotransduction of seeded or surrounding cells, thereby promoting both osseointegration at the scaffold interface and tissue differentiation into bone as the scaffold degrades [22, 23]. Yet throughout the myriad of approaches considered, limitations remain in achieving the balance between structure, mechanical behavior and function needed to ensure both load bearing requirements upon implantation and susceptibility to resorption for gradual bone regeneration [24]. Specifically, the frequent failure of these resorbable scaffolds upon implantation to defect sites can often be attributed to insufficient integration due to poor vascularization [21]. Thus, despite a steadily increasing bone graft substitute market, factor- and cell-based grafts, which have the greatest potential for personalized regeneration, still lag behind non-resorbable grafts and allografts [25].

The preponderance of bone defects today, occasioned by a growing exercise trend, an aging population and an increased incidence of bone-weakening conditions including osteoporosis and diabetes mellitus [26, 27], has therefore escalated the unmet need for a bone repair strategy capable of complete regeneration.

1.3. The endochondral ossification approach

Recently, in light of shortcomings with respect to vascularization and integration in efforts to engineer bone, some investigators have turned their attention to the native bone defect repair pathway, known as endochondral ossification. In this process, ruptured vessel leakage at

initial site of injury leads to the formation of a hematoma (fibrin clot) which becomes a center of inflammation due to the release of TGF-β1 and PDGF by platelets [28]. Over the following 24 hours, recruited macrophages secreting TNF-α and IL-1 promote the invasion of blood vessels along with fibroblasts and osteochondroprogenitor cells which transform the hematoma into granulation tissue and subsequently, a fibrocartilaginous matrix known as a soft callous [28, 29]. The chondrocytes present in this matrix then proliferate, become hypertrophic, and mineralize their surrounding environment before undergoing apoptosis. Concurrently, invading blood vessels precipitate bone formation through vascularization as well as the recruitment of remodeling osteoclasts and bone forming osteoblasts [29, 30], gradually leading to the formation of a hard callus and, finally, trabecular bone tissue. This process resembles quite closely the embryonic development of long bones with the added involvement of inflammation [28, 31]. Furthermore, endochondral ossification hinges on the precise sequential and targeted delivery of a number of cytokines, proteins and growth factors, including angiogenic factors such as VEGF, matrix degrading proteases such as MMPs, as well as chondrogenic and osteogenic factors such as BMP-2 [29].

In an attempt to engineer the repair pathway rather than the tissue itself, an increasing number of studies in recent years have sought to mimic this endochondral ossification process for bone regeneration. Since endochondral ossification is endogenous to long bones during development and most widely studied in long bones for repair [30, 32], these efforts remain mostly within the purview of long bone defect regeneration. There are currently numerous approaches aiming to replicate endochondral ossification, all of which consist in generating a cartilage template using chondrocytes or MSCs as well as various bioconjugation methods and biomaterials. These existing techniques include employing pure MSC aggregates which are

differentiated using chondrogenic medium [33], MSCs encapsulated in hydrogel casts [34, 35], MSCs seeded onto porous scaffolds [36, 37] and MSCs bioprinted into simple lattice or non-porous structures [38-40].

Throughout these studies, cartilage-like templates susceptible to ossification upon implantation show greater success with bone defect repair compared to cell-laden scaffolds ushered down a direct osteogenic pathway [35, 41]. Taken together with the extensive link previously established between hypertrophic chondrocytes and VEGF secretion vital to vessel ingrowth [41], these studies point to vascularization as being both a primary determinant of bone regeneration outcome and the main discriminant between scaffolds designated for either direct osteogenesis or endochondral ossification. We note however that, though all these studies devise specific delivery sequences of cytokines and growth factors to drive scaffolds down the multi-step ossification pathway, they do not establish the spatial control needed to recapitulate the regional heterogeneity of the ossification milieu. Indeed, since vessel invasion occurs progressively from the outer edges of the callus, the active area of ossification corresponds to an interface between callus tissue and bone which shifts gradually further into the callus until the defect is fully healed [28, 42, 43]. Thus, the ossification milieu consists of dynamic yet regionally organized elements characterized by specific structures, mechanical properties and material behaviors.

1.4. Additive manufacturing as a biofabrication technology

Additive manufacturing techniques, also known as 3D printing, allow for precise spatial control in the fabrication of tissue constructs. Indeed, bioprinting, which generates constructs

through layer-by-layer deposition of cell-laden hydrogel material, has emerged as an advantageous approach over more traditional methods, such as molding, that do not offer sufficient control over the intricacies associated with engineering complex tissues [44]. In particular, bioprinting has the potential to allow for the encapsulation and patterning of multiple cell types as well as to ensure accurate control over construct geometry at the microenvironmental level. Though current bioprinting approaches include inkjet and laser-assisted printing, extrusion printing has become an appealing option for biofabrication due to its affordability, capacity for high cell density and adaptability for materials, specifically hydrogels, with a diverse range of properties (viscosity, crosslinking/solidification method, etc.) [45-48].

Additive manufacturing is especially suited to bone defect repair since it is capable of rapidly generating individual scaffolds with bulk shapes which fit the boundaries of each targeted defect, making it a feasible fabrication technique for both prototyping and testing as well as scaled-up personalized production. Moreover, through the use of multiple extrusion heads, this technology is capable of producing multi-material scaffolds, most notably cell-laden or factor-conjugated hydrogels reinforced with stiff thermoplastic networks. Noting these advantages, Daly *et al.* most recently fabricated hypertrophic cartilage templates from porous MSC-laden hydrogels reinforced with polycaprolactone (PCL) suitable for bone engineering through implantation [49]. Though it did validate additive manufacturing as a promising biofabrication strategy for bone defect repair, the study did not investigate the specific impact of the extrusion process itself on defect outcome nor did it evaluate the role of material behavior and architecture by modulating geometric parameters including pore size as well as hydrogel and PCL strut sizes.

In order to develop robust, consistent and scalable biofabrication platforms, some efforts have certainly been made to characterize the impact of bioprinting parameters, including printing speed and pressure as well as needle diameter, on extruded construct properties such as resolution [50, 51]. However, investigation into the mechanical behaviour of extruded constructs as compared to conventional biofabrication techniques remains lacking. Indeed, previous mechanical characterization studies of extruded constructs are largely constrained to the elastic component of construct behaviour [52-54] and do not extend to evaluating the mechanism behind differences in both elastic and time-dependent mechanical properties resulting from the bioprinting process itself [55]. Another crucial characteristic of scaffolds, most notably hydrogels, which remains unexplored with respect to additive manufacturing is the capacity to undergo swelling and shrinking as a result of fluid flow in response to imbalances between osmotic or mechanical pressure, electrostatic forces and elastic restoring forces [56, 57].

Given these gaps in the literature, the application of additive manufacturing to bone defect repair warrants a preliminary identification of properties most crucial to the ossification process, followed by an investigation of the specific impact of the additive manufacturing process on these properties, and culminating in the establishment of precise control over these properties through the modulation of printing parameters.

1.4. Construct property considerations

1.4.1. Structure and mechanical behavior

Arguably the most influential and certainly most evident characteristic governing the

development, homeostasis and repair of bone is mechanical behavior, a property which is

determined not only by material composition but also by structure [58]. Notably, it has been

widely established that the microstructure of trabecular bone, which is comprised of a tortuous

network of interconnected rod and plate elements [59, 60], plays a critical role in determining

stress distribution profiles experienced during mechanical loading [61]. Furthermore, the effects

of regional mechanical stresses on endochondral ossification have previously been demonstrated

extensively [62-64]. In addition, as previously mentioned, the ossification process does not take

place uniformly across the callus tissue, but rather progresses inwards from the outer edges [28,

42, 43], an occurrence which very likely depends in part on regional differences in structural and

mechanical properties. Taken together, these findings underline the pivotal role of structure and

mechanical behavior for cartilage templates in their outcome vis-à-vis ossification. Moreover,

the importance of mechanical behavior in endochondral ossification engineering is further

supported by implantation considerations for the cartilage template since hydrogels alone are not

sufficiently strong. Reinforcements that raise the bulk modulus of the template whilst

maintaining adequate strength for a sufficiently high fracture strain are indeed needed to properly

affix implant to bone using existing surgical methods, which include press fitting and attachment

to fixation plates [11, 65, 66].

1.4.2. Swelling behavior

Another hallmark phenomenon associated with endochondral ossification as well as other injuries involving inflammation is swelling, which occurs as ruptured vessel leakage and fluid accumulation at a site of injury contributes to tissue turgescence. Findings that swelling is linked and likely contributes to heterotopic ossification in soft tissues underline fluid flow as being a potentially important regulator in endochondral ossification [67]. Less directly, swelling is known to also impact mechanical behavior, most notably time-dependent mechanical properties, since, in cartilage-like constructs, water flow governs stress relaxation [68] and since, in native cartilage, glycosaminoglycans (GAGs) create swelling pressure through repulsion between negatively charged components to ensure adequate mechanical responses to loading [69]. Despite these clear indirect and putative direct roles in endochondral ossification, swelling may also cause unwanted deformation which may affect structural, compositional and mechanical properties in hydrogel-based scaffolds, thereby disrupting the engineered repair process [70].

1.4.1. Porosity

Finally, porosity is also a key characteristic of both bone and cartilage tissues as well as their engineered construct counterparts [71]. Indeed, as previously discussed, the architecture of a trabecular bone network, which is mirrored in and tantamount to the complementing macro-scale porosity network, dictates regional stress distribution profiles during mechanical loading [61]. Similarly, in engineered cartilage constructs, it is in fact the microporous network that determines the rate and extent of fluid flow through each construct, and consequently the time-dependent mechanical properties of each construct [68]. In addition to these microporous networks which also control the transport of nutrients and waste, engineered constructs also

possess maco-scale pores (1) to raise the fluid content available to the constructs by increasing both the fluid reservoir volume and the surface area of exposure to fluids, and (2) to accommodate seeded cells, newly formed tissue and invading vasculature for construct integration and remodeling [68, 72]. Moreover, parameters such as porosity, pore size and pore interconnectedness have been shown to affect rates of scaffold degradation, a process which must be tuned to match the rate of tissue formation [71].

If follows from these findings that, for different materials, various types of porosities across a range of spatial scales amount to distinct mechanisms for mechanical reinforcement, fluid uptake and molecular transport. In soft materials, micropores may mimic the role of GAGs in controlling mechanical response through fluid flow while macropores may contribute to water uptake into the structure which in turn constitutes another mechanism of bulk volumetric swelling and deformation. In stiff materials, micropores may increase susceptibility to fracture [73] while macropores determine bulk elastic moduli and stress distributions during loading, much like in trabecular bone. Therefore, given that the active site of ossification during native bone repair is an interface between stiff bone material and soft cartilage-like callus material, there exists a tight interplay between properties relating to mechanical behavior, swelling and porosity which will be at play in constructs targeting bone repair through endochondral ossification.

1.5. Description of proposed approach

In light of the largely unexplored relationship between the mechanical behavior, swelling and porosity of engineered cartilage templates, especially in the context of using additive

manufacturing, we propose to develop a 3D printing-based biofabrication method for cartilage templates through a careful, parameter-driven study. This study will aim to concurrently probe the impact of extrusion on mechanical behavior, swelling and porosity in order to establish control over these properties through printing parameters as well as to inform decisions about the cartilage template fabrication strategy.

As both an exercise in translational design and a foundation for the later establishment of design criteria and constraints, we've also laid forth a multi-step personalized intervention strategy for critical bone defects resulting from trauma, cancer or infection, as illustrated in Figure 1. We first envision a preliminary intervention whereby the site of injury is immobilized using existing techniques at the discretion of the orthopedic surgeon (ex: compression plates, intramedullary rods or Kirschner wires). Using defect boundary conditions obtained from 3D imaging, most likely CT-scanning, as well as mesenchymal stem cells isolated from the patient's lipoaspirate [74] and differentiated into chondrocytes, engineered constructs would then be produced in accordance with the developed 3D printing-based biofabrication method. Consisting of a porous chondrocyte-laden hydrogel reinforced with a stiff network and shaped to fit the site of injury, each tailored construct is subsequently cultured until mature cartilage tissue replaces the hydrogel scaffold, at which point the construct is implanted to the site of injury and held in place through press fitting and compression plate fixation. Once the construct is fully ossified and integrated into the surrounding bone, the compression plates may finally be surgically removed. In addition to (1) the tailorability that 3D printing offers in terms of bulk geometry, porosity architecture, mechanical behavior and fluid flow, as well as (2) the improved vascularization, ossification and integration that endochondral ossification provides compared to direct osteogenesis, the proposed approach employs the patient's own cells, precluding the

possibility of rejection, and the implanted scaffold is intended to fully resorb, leaving only native

tissue devoid of foreign materials used for fixation or support.
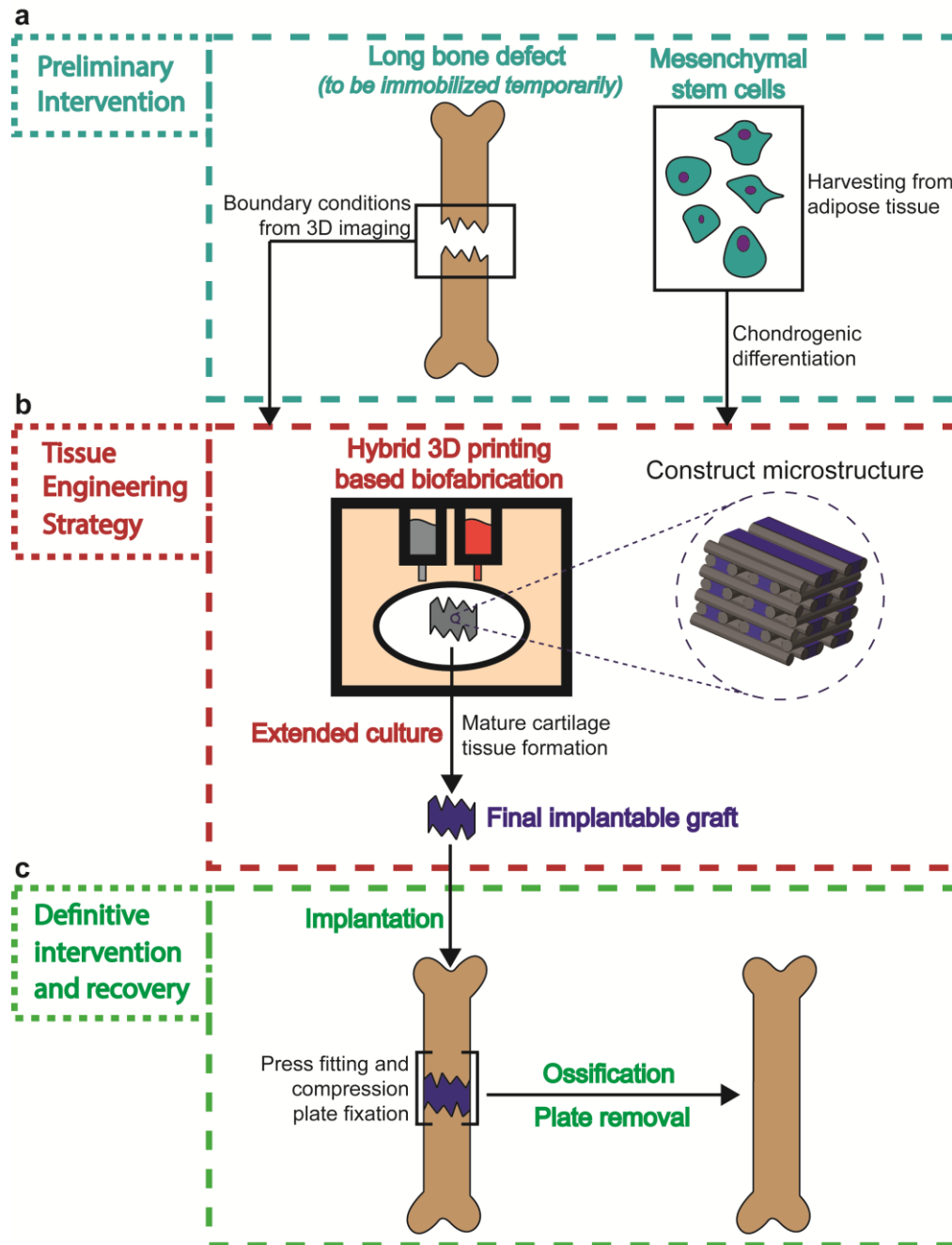
Figure 1. Proposed approach to critical bone defect repair. (a) A patient suffering from a long bone defect first undergoes an emergency surgery to immobilize the defect area (using compression plates, rods, nails, casts…). 3D imaging outlining defect boundaries (ex: CT scanning) is performed. In addition, the patient's mesenchymal cells are harvested from adipose tissue through liposuction and differentiated into chondrocytes. (b) The boundary conditions and obtained chondrocytes are employed to construct a

customized cartilage template by printing a hybrid scaffold, consisting of a stiff support structure and a cell-laden hydrogel network, and subsequently culturing the scaffold for tissue maturation. (c) The generated graft is implanted to the defect area and immobilized using press fitting, made possible by the stiff network within the scaffold, and compression plates. Following successful integration and ossification of the fabricated graft, compression plates are removed, leaving a fully healed long bone devoid of foreign material.

2. Overview of aims

The overall goal of developing a 3D printing-based biofabrication method for cartilage templates through a careful, parameter-driven study was divided into two aims:

Aim 1: Assess the specific impact of the extrusion process on construct properties, most notably microstructure, mechanical behavior and swelling, as they relate to bioprinting parameters and establish parametric control over the 3D printing process.

Aim 2: Develop a cartilage template biofabrication strategy informed by the findings of Aim 1 and revolving around 3D printing, and investigate the parameter-dependent structural, mechanical and swelling behavior of generated constructs.

3. Aim 1

3.1. Experimental design and material selection

The objective of this aim was to gain a mechanistic understanding of how bioprinting affects the mechanical and swelling properties of extruded hydrogel constructs as part of a characterization evaluating the impact of both hydrogel composition and bioprinting parameters on construct properties. The employed biofabrication platform consists of a BioBots Beta pneumatic extruder in combination with gelatin methacrylate (GelMA) (Figure 2a and b).

GelMA was chosen because it is a widely-used bioink for extrusion [75, 76] that contains cell-binding RGD motifs [77] and supports encapsulated cell viability [54, 78]. We modulated parameters including polymer content, photocrosslinking initiator concentration, printing speed, nozzle inner diameter and printing pressure (Figure 2c). Construct quality and resolution were evaluated using optical microscopy. Cell viability of cells encapsulated in extruded and molded constructs was using LIVE/DEAD® staining. Then, hydrogel cylinders of the exact same dimensions were prepared by molding or extrusion and uniaxial unconfined compression was performed to assess differences in Young's modulus (Figure 2d). Differences in time-dependent mechanical properties between extruded and molded constructs were subsequently assessed in unconfined creep, an established if preliminary method for the characterization of viscoelastic and poroelastic materials [79-81]. Finally, the mechanism by which extrusion altered the mechanical properties of constructs was examined using optical microscopy and a swelling kinetics study. Taken together, the results of this investigation provide critical information as to how the bioprinting process modulates the performance of extruded constructs under mechanical stimulation.
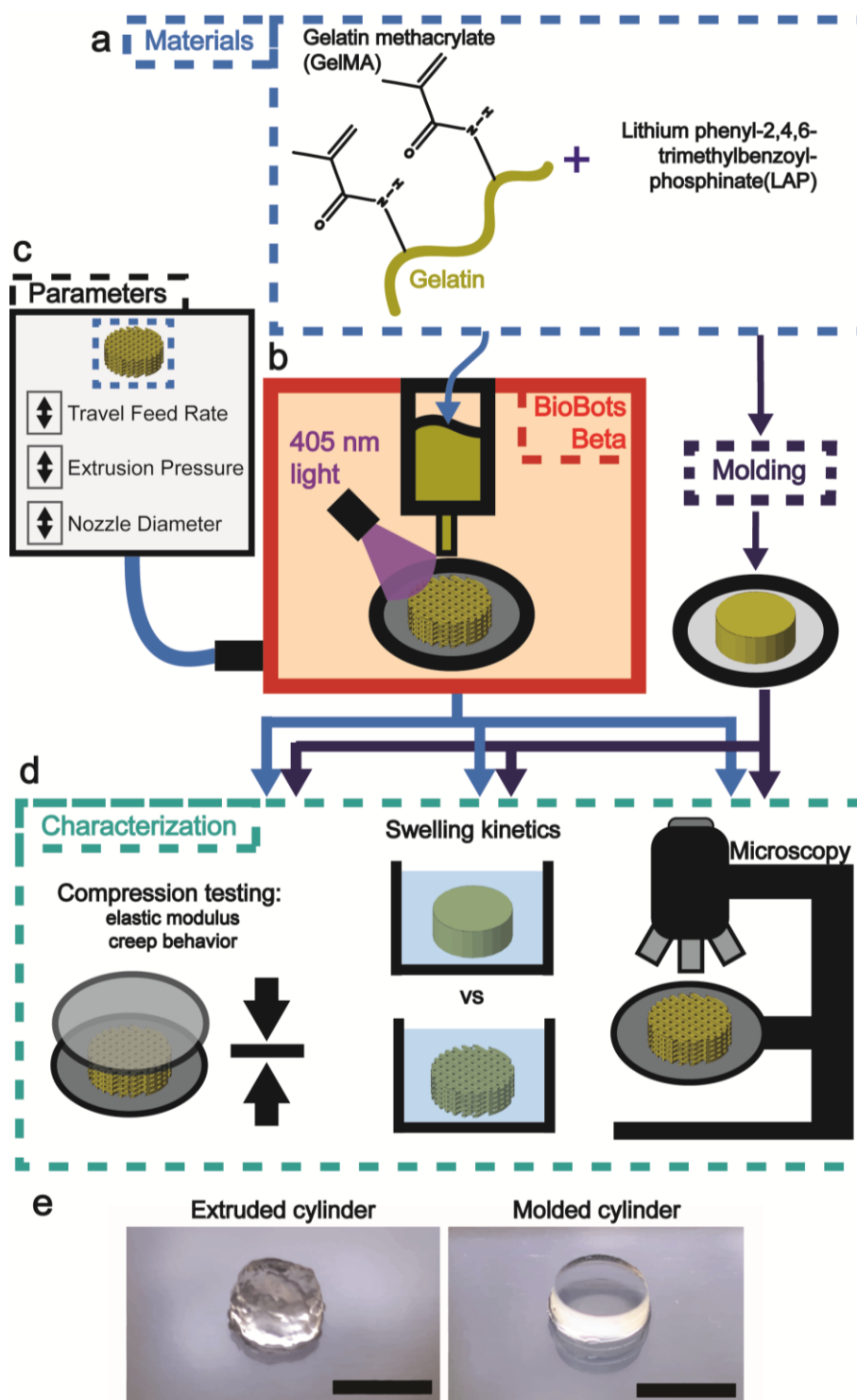
Figure 2. Experimental design for Aim 1. (a) Various formulations of gelatin methacrylate (GelMA) hydrogel photocrosslinked with lithium phenyl-2,4,6-trimethylbenzoylphosphinate (LAP) were extruded into different structures (b) at varying travel feed rates, nozzle diameters and extrusion pressures (c). (d) Hydrogels with the same dimensions were prepared, and (e) hydrated unconfined compression testing, a swelling study, and optical microscopy were used to evaluate construct properties for comparison against molded counterparts prepared with the exact same dimensions. Scale bars: 5 mm.

3.2. Methods

3.2.1. Gelatin methacrylation

GelMA was synthesized using previously described methods [75, 76]. Briefly, a 10% w/v

solution was prepared by dissolving gelatin (Type A, 300 bloom, porcine skin, Sigma Aldrich) in

phosphate buffered saline (PBS) at approximately 60°C. Following complete dissolution, the

solution temperature was maintained at 50°C and 0.14 mL methacrylic anhydride was added for

each gram of dissolved gelatin. The methacrylation reaction was allowed to proceed for 4 hours

at 50°C under vigorous stirring. PBS warmed to 40°C was added to obtain a GelMA

concentration of 4.5% w/v, and then ice-cold acetone was added at a volumetric GelMA

solution-to-acetone ratio of 1:4, allowing the GelMA to precipitate overnight. The precipitate

was dried and dissolved in PBS at a concentration of 10% w/v by heating to approximately 50°C.

Following vacuum filtration through a 0.22 μm filter (polyethersulfone membrane, Fisher

Scientific), the solution was dialyzed (Slide-A-Lyzer G2 Dialysis Cassettes, gamma-irradiated,

10K molecular weight cutoff, Fisher Scientific) for 3 days against deionized water with dialysis

media change twice a day. The GelMA solution was finally lyophilized for four days and stored

at -20°C.

3.2.2. Hydrogel fabrication by bioprinting and molding

Lithium phenyl-2,4,6-trimethylbenzoylphosphinate (LAP), a cytocompatible

photoinitiator activated by visible light at a wavelength of 405 nm [82, 83], was used to initiate

photocrosslinking of GelMA. Hydrogels were prepared by dissolving synthesized GelMA at 10-

20 w/v% in PBS along with LAP (Biobots) at 0.25% or 0.5%, as indicated. The employed

bioprinting system was a BioBots Beta pneumatic extruder, which is equipped with an extrusion

pressure range of 0-140 psi and violet light irradiation capability at a wavelength of 405 nm. Prepared hydrogel formulations were loaded in a 10 mL syringe (BD) fitted with 27 gauge (27G, 200 μm inner diameter), 22 gauge (22G, 420 μm inner diameter) or 18 gauge (18G, 840 μm inner diameter) nozzles (Jensen Global Dispensing) for extrusion. Solutions were allowed to physically crosslink (gel) in the syringe prior to extrusion (~20min). Computer models for the constructs (either lines or cylinders) were designed using Creo Parametric 3.0 and imported into Repetier-Host software, where printing speed was set prior to extrusion. Hydrogel lines were extruded at printing pressures ranging from 60 to 130 psi and travel feed rates from 4 to 12 mm/sec, as indicated, under constant irradiation from the violet light source. Hydrogel cylinders were printed at 100 psi, 8 mm/sec, and in 6 layers.

Molded cylinders of the exact same dimensions as extruded cylinders were prepared by letting GelMA solutions gelate at solution depths matching that of extruded counterparts for 20 min and then irradiating the solutions under violet light for the same amount of time as extruded cylinders (10 min). Biopsy punches (Fisher Scientific) were subsequently used to obtain molded cylinders with the exact same dimensions as extruded cylinders (1.4 mm height x 5 mm in diameter). Petri dishes were used as extrusion and molding substrates for extrusion pressure testing, line width evaluation, all mechanical testing and the swelling study, while glass slides were used for the microstructural analysis of constructs with optical microscopy.

3.2.3. Imaging and analysis for line extrusions and cylinders

Single-layer extruded lines were imaged using an EVOS microscope (transmitted light, phase contrast, 4x magnification). For line extrusions with 18G nozzles, whose widths exceeded the imaging area of the microsope, full-size images of each line were generated by capturing two

images spanning the total width and performing a stitching operation using ImageJ [84]. The total area of each line (obtained from ImageJ) was divided by the total length to obtain the average line width.

Representative photographs of extruded and molded cylinders were taken with a Canon S120 digital camera. Using a Zeiss AxioObserver Z1 microscope (phase contrast, 10x magnification), optical micrographs of extruded and molded cylinders (15 mm diameter, 1 mm height) were also taken to assess differences in microstructure. The focal plane of the micrographs was set to the surface of the glass, i.e. the plane of contact between the hydrogel and the glass substrate.

3.2.4. Cell culture

Although high viability of cells encapsulated in gels prepared with similar crosslinking protocols, including the use of GelMA, LAP, and light exposure for up to 10min, have been described in several studies [82, 83, 85], we conducted a cell viability assay to assess the impact of the extrusion process on cell viability. NIH/3T3 fibroblasts (ATCC® CRL-1658™) were cultured in Dulbecco's Modified Eagle's Medium (DMEM) with 4.5g/M glucose, L-glutamine, and sodium pyruvate (Corning, Corning, NY, Cat. No. 10-013) supplemented with 10% heat-inactivated fetal bovine serum and maintained in an incubator at 37°C and 5% CO2. Cells were subcultured when approximately 80% confluent and detached using trypsin-EDTA (0.25%, phenol red) (ThermoFisher Scientific, Waltham, MA Cat. No. 25200056). Culture medium was changed every 3-4 days. The baseline viability of the cells was assessed using the Trypan Blue Exclusion method prior to encapsulation and the LIVE/DEAD® assay.

3.2.5. Cell encapsulation and viability study

Concentrated stock solutions of cells and GelMA (maintained at 37°C) were gently

mixed together resulting in a final concentration of 10% GelMA and 5.0 x 10^5 cells/mL. For the

creation of 3D printed constructs, approximately 5mL of cell-laden GelMA was poured into a 10

mL syringe and allowed to cool for 20 minutes. Next, eight lines were 3D printed using a 27G

nozzle, a travel feed rate of 8mm/sec, and a layer height of 0.2 mm onto a microscope slide

before being exposed to 405 nm light for 10 minutes. For the creation of molded hydrogels, 1mL

of cell-laden GelMA was poured into one well of a 6-well plate and allowed to cool for 20

minutes. The thickness of the hydrogel approximated the thickness of the extruded lines

described above. A 5 mm biopsy punch was used to obtain molded hydrogels, which were then

were placed on a microscope slide and exposed to 405 nm light for 10 minutes. Cell viability was

immediately assessed using the LIVE/DEAD® assay (Thermo Fisher Scientific) according to the

manufacturers' instructions. Briefly, the two components were combined with sterile PBS to

generate 2 mL of a 4 μm ethidium homodimer (EthD-1) and 2 μm calcein AM solution. Live

cells were stained with calcein AM (excitation/emission (ex/em): ~495nm/~515nm) and

damaged or dead cells were stained with EthD-1 (ex/em: ~495nm/~635). Hydrogels, encircled

with a hydrophobic pen, were incubated with 100-150 μL of LIVE/DEAD® solution for 20

minutes at room temperature. Cells not subjected to hydrogel encapsulation were used as a

positive control.

3.2.6. Cell-laden hydrogel imaging acquisition and analysis

One image of each sample (n=5 for all groups: 3D printed, molded, and positive cell-only

control) was immediately captured using confocal microscopy (Zeiss LSM 700, Peabody, MA).

A z-stack of images (a minimum of n=20 per sample), standardized to image through the entire thickness of the sample, was captured through the microscope slides using a resolution of 512 x 512 pixels via a 10x/0.3 Dry lens, 5% laser output using the 488nm and 639nm lasers, and a pinhole of 1AU. Images were processed using ImageJ, where Z-stacks were compressed into one image using maximum intensity and subsequently subtracting the background using a rolling ball algorithm [86]. Subsequently, images were converted to RGB, channels were split to manually count dead (red) and live (green) cells using the ImageJ Cell Counter plugin. Percent viability was determined by dividing the number of live cells by the total number of cells and multiplying by 100%.

3.2.7. Mechanical testing

For mechanical testing, cylinders (5 mm diameter, 1.4 mm height) were placed on the compression platens of a Bose Electroforce 3220 in an unconfined setup, immersed in PBS, and preloaded with a compressive stress of 2.5 kPa prior to each test. To measure Young's modulus, hydrogels were uniaxially compressed to a strain of 15% at a strain rate of 10 or 16.5% per minute, as indicated. Linear regression was performed on the obtained stress-strain data over the initial 7% of strain [87] to obtain the slope of the initial linear portion of the stress-strain curve (Young's modulus). For creep testing, a 5 kPa stress was applied to the cylinders for 7 minutes (creep portion) followed by reduction of stress to 2.5kPa for 7 minutes (recovery portion). Exponential fitting of the creep and recovery portions of the data was performed using equations (1) and (2) respectively, where ε represents strain. Note that t corresponds to elapsed time from the moment at which a stress of 5 kPa was reached for equation (1) and the moment at which a stress of 0 Pa was reached for equation (2). a_{creep} and $a_{recovery}$ correspond to the changes in strain caused by creep and recovery respectively while b_{creep} and $b_{recovery}$ correspond to the equilibrium

strain values of the creep and recovery portions respectively. τ is a time constant that corresponds roughly to the amount of time it takes for the strain to reach around 37% of its final value (1/e).

$$\varepsilon(t) = a_{creep} \, \exp\left(-\frac{t}{\tau_{creep}}\right) + b_{creep} \qquad (1)$$

$$\varepsilon(t) = -a_{recovery} \, \exp\left(-\frac{t}{\tau_{creep}}\right) + b_{recovery} \qquad (2)$$

From the fitting, time-dependent mechanical behaviour was quantified using four properties, namely extent of creep, average creep rate, extent of recovery and average recovery rate. The extent of creep is the total change in strain caused by creep while the extent of recovery is the percentage of this strain change that is recovered during unloading. Average creep and recovery rates correspond to the average rates of change in strain over the initial 99% of creep and recovery respectively.

3.2.8. Swelling kinetics

A swelling kinetics study was performed to assess the impact of microstructural differences on fluid flow. Molded and extruded cylinders (5 mm diameter, 1.4 mm height) were prepared and their exact dimensions (diameter and height) were measured with calipers before they were fully dried. For each cylinder, the polymer density was calculated by dividing the dry weight of the cylinder by the volume of the cylinder obtained from the dimensional measurements. After drying, cylinders were immersed in 10 mL PBS and weighed at multiple time points over 5 days of swelling. Swelling percentage was calculated using equation (3), where M_t corresponds to the hydrogel mass at time t and M_0 corresponds to the initial weight of the dried polymer prior to immersion in PBS.

$$\text{Swelling percentage} = \frac{M_t - M_0}{M_0} \times 100\% \tag{3}$$

3.2.9. Statistical analysis

Two way-ANOVA with post-hoc Tukey analysis was performed to determine statistical significance between groups in the line width vs travel feed rate data and the Young's modulus vs biomaterial composition data. One way-ANOVA with post-hoc Tukey analysis was performed to determine statistical significance between groups in the cell viability data. Two-tailed t-tests were performed to compare Young's moduli, creep parameters and polymer density data between extruded and molded cylinders. A two-tailed t-test with Holm-Sidak correction for multiple comparisons was performed on extruded and molded groups in the swelling percentage data. All data are shown as mean ± SEM, with n=8 for all line width data, n=5 for cell viability data and n=6 for all mechanical testing and swelling data. All graphs were plotted using GraphPad Prism 6 software. A p-value of less than 0.05 was considered statistically significant.

3.3. Results

3.3.1. Combinatorial effects of extrusion parameters and biomaterial composition on construct quality and resolution

Qualitative characterization of extruded lines (Figure 3) revealed the existence of an optimal extruding pressure at each GelMA concentration investigated (Table 1). For each GelMA concentration, extrusion skips were observed at pressures below the optimal range while unevenly excessive outpour was observed above that range.
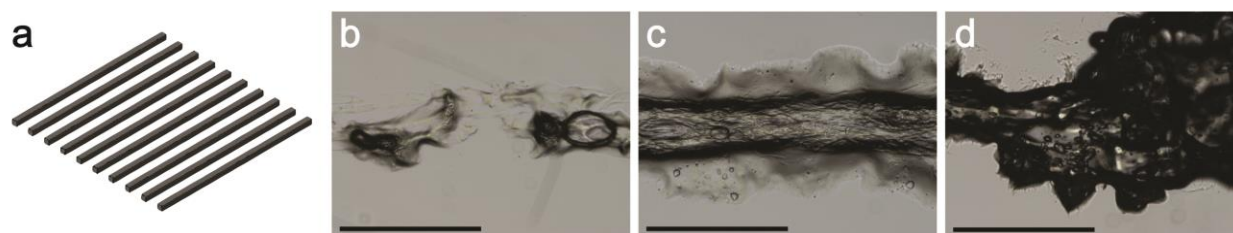
Figure 3. Optimal extruding pressure is dependent on biomaterial composition. (a) Sequential lines, as shown byCADmodel, were extruded at various concentrations (10%, 15% and 20%w/v GelMA) and pressures (0–140 psi) with a 27G nozzle. LAP concentration was 0.5%w/v and travel feed rate was 8 mm s−1. Micrographs shown are representative of line extrusions at 60 psi (b), 80 psi (c) and 100 psi (d) for 10% GelMA/0.25% LAP. Scale bars: 1000 μm.

Table 1. Qualitative characterization of line extrusions reveals the existence of optimal GelMA concentration/extrusion pressure pairings. * Required extrusion pressure exceeds maximal capabilities.

	Non-continuous flow, uneven thickness: beads instead of lines	Optimal pressure, continuous flow, constant thickness	Excessive outpour, uneven thickness, large chunks in lines
10% w/v GelMA	60 psi	80 psi	100 psi
15% w/v GelMA	80 psi	100-110 psi	120 psi
20% w/v GelMA	100 psi	130 psi	--*

The impact of printing speed on line resolution was assessed by extruding lines at travel feed rates of 4 mm/sec, 8 mm/sec and 12 mm/sec. The impact of nozzle inner diameter was also evaluated by extruding lines with 27G, 22G and 18G nozzles. As expected, increasing the travel feed rate resulted in a significant decrease in line width, corresponding to an increase in resolution ($p<0.0001$ for travel feed rate factor in two-way ANOVA, Figure 4a,c) while increasing the inner diameter of the nozzle significantly increased line width ($p<0.0001$ for one way ANOVA, Figure 4b,d). Interestingly, increasing the GelMA concentration from 10% to 20% w/v also resulted in a small but significant decrease in line width ($p<0.05$ for GelMA concentration factor in two way ANOVA).
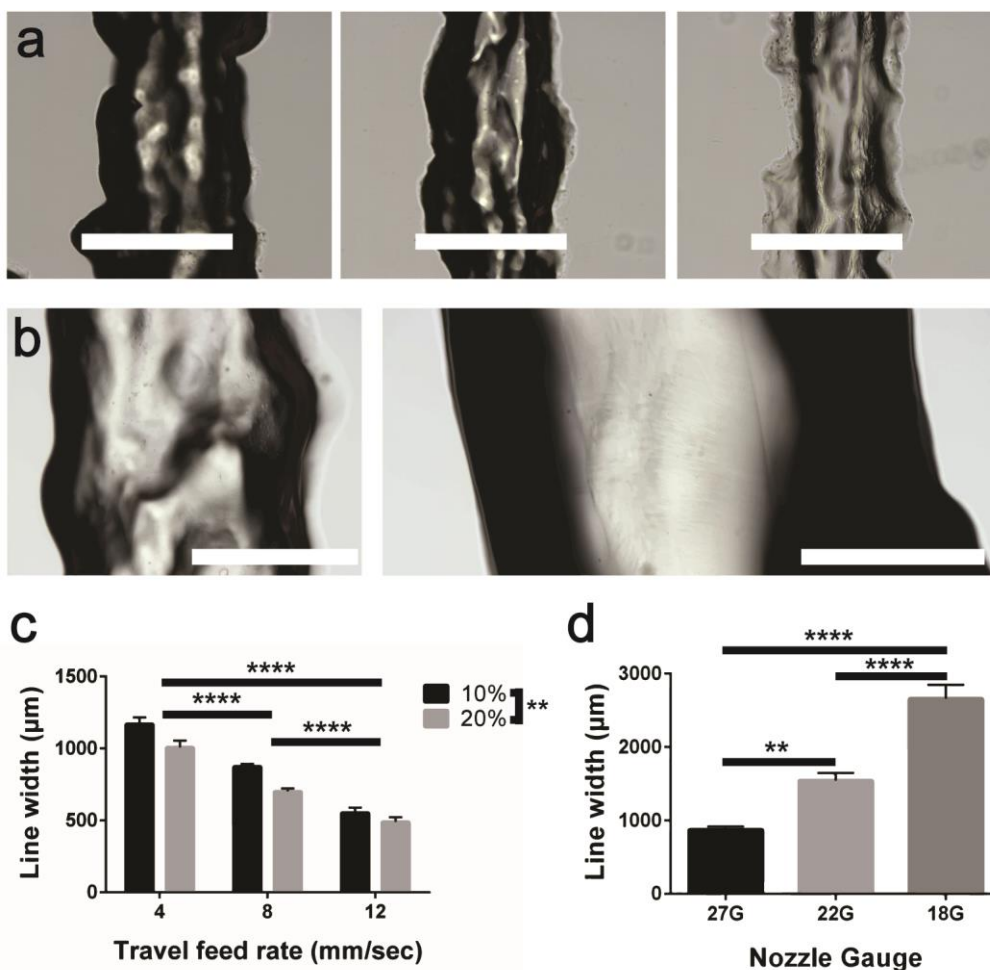
Figure 4. Both travel feed rate and biomaterial composition modulate extrusion resolution, measured by line thickness. (a) Representative images shown for line extrusions at 4 mm s−1 (left), 8 mm s−1 (center) and 12 mm s−1 (right) for 10% GelMA/0.25% LAP. Scale bars: 1000 μm. (b) Representative images shown for line extrusions with a 22G nozzle at the optimal pressure of 40 psi (left) and with an 18G nozzle at the optimal pressure of 10 psi (right) for 10% GelMA/0.25% LAP and a travel feed rate of 8 mm s−1. Scale bars: 1000 μm. (c) Line thickness data as a function of GelMA concentration (10% or 20%) and travel feed rate, quantified by micrograph analysis (**p ≤ 0.0001, two way ANOVA and Tukey post hoc analysis). (d) Line thickness data as a function of nozzle gauge quantified by micrograph analysis (**p≤0.01, ****p ≤ 0.0001, one way ANOVA and Tukey post hoc analysis).**

3.3.3. Cell viability study

To confirm the cytocompatibility of the employed extrusion and photocrosslinking methods, a LIVE/DEAD® assay was performed immediately after the preparation of molded and extruded constructs encapsulated with 3T3 cells. Cell viability was high (~95%) for cells

encapsulated in extruded constructs and molded constructs, as well as for unencapsulated controls, with no significant differences between any of the experimental groups (Figure 5). There were no significant differences in cell viability between these three groups and the baseline cell viability measured by Trypan blue exclusion prior to encapsulation and the LIVE/DEAD® assay, which was 97.27% ± 1.12%.

3.3.3. Impact of extrusion process on bulk mechanical properties

As expected, increasing the GelMA concentration from 10% to 15% and 20% resulted in an increase in the Young's modulus of molded cylinders (Figure 6b). The concentrations of the photoinitiator (LAP) investigated here had no effect on hydrogel elastic behavior.

The impact of extrusion on Young's modulus was assessed by comparing molded and extruded hydrogel cylinders prepared with 15% GelMA and 0.25% LAP. Surprisingly, while no differences were observed in Young's modulus between molded and extruded cylinders (Figure 6c), extruded constructs exhibited increased extents (Figure 7b) and rates of creep (Figure 7c) compared to molded constructs. Moreover, while the extent of recovery from creep was not different between extruded and molded constructs (Figure 7d), the rate of recovery from creep was higher for extruded constructs (Figure 7e). These results indicate that the extrusion process did not affect bulk elastic behaviour (Young's modulus), but time-dependent mechanical behaviour was affected.
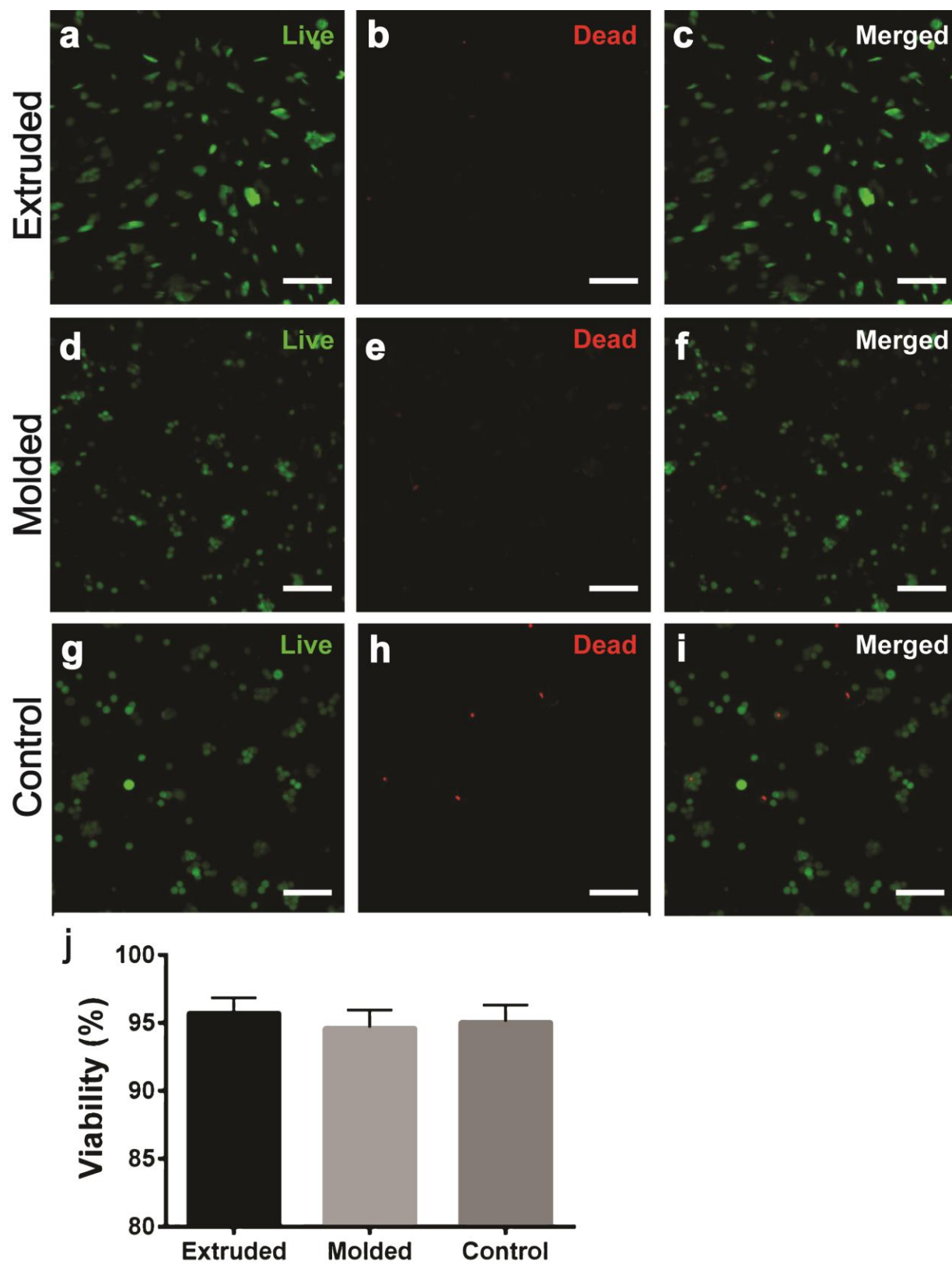
Figure 5. Cell viability was not affected by 3D printing process. (a)–(c) 3D printed hydrogel lines; (d)–(f) molded hydrogels; (g)–(i) cell-only controls. (j) Quantitative analysis of cell viability. Scale bars are 100 μm.
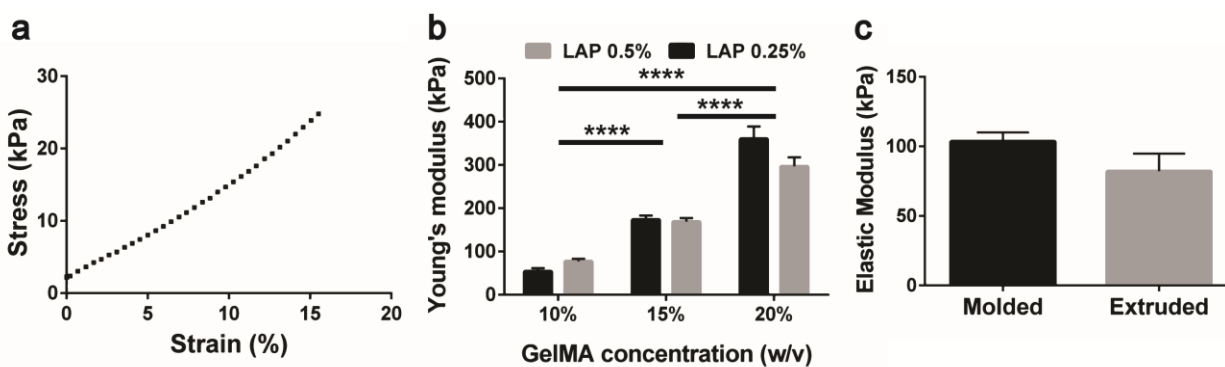
Figure 6. Elastic deformation behavior is modulated by biomaterial composition but not by printing itself. (a) Representative portion of stress/strain data from unconfined compression. (b) Young's moduli of hydrogels prepared with 10%, 15%, 20% GelMA and 0.25%, 0.5% LAP (**p ≤ 0.0001). There was no significant difference between hydrogels prepared with 0.25% and 0.5% LAP. (c) Young's moduli of printed and molded GelMA cylinders (15% GelMA, 0.25% LAP). Note that elastic moduli in (b) were measured in uniaxial compression with a strain rate of 10%/min, while elastic moduli in (c) were measured using a strain rate of 16.5%/min.**

3.3.4. Impact of extrusion process on microstructure and swelling properties

To investigate the mechanism behind the observed differences in time-dependent mechanical properties, molded and extruded cylinders were imaged under phase contrast microscopy. Molded constructs were characterized by uniform light transmission through the hydrogel (Figure 8a) while extruded constructs were characterized by a microstructure with extensive refraction (Figure 8b). Surprisingly, although extruded and molded hydrogels had similar polymer densities (Figure 8c) upon fabrication, differences in swelling behaviour between extruded and molded constructs were apparent after 1 day, with extruded constructs exhibiting both faster and more extensive swelling compared to molded counterparts (Figure 7d).
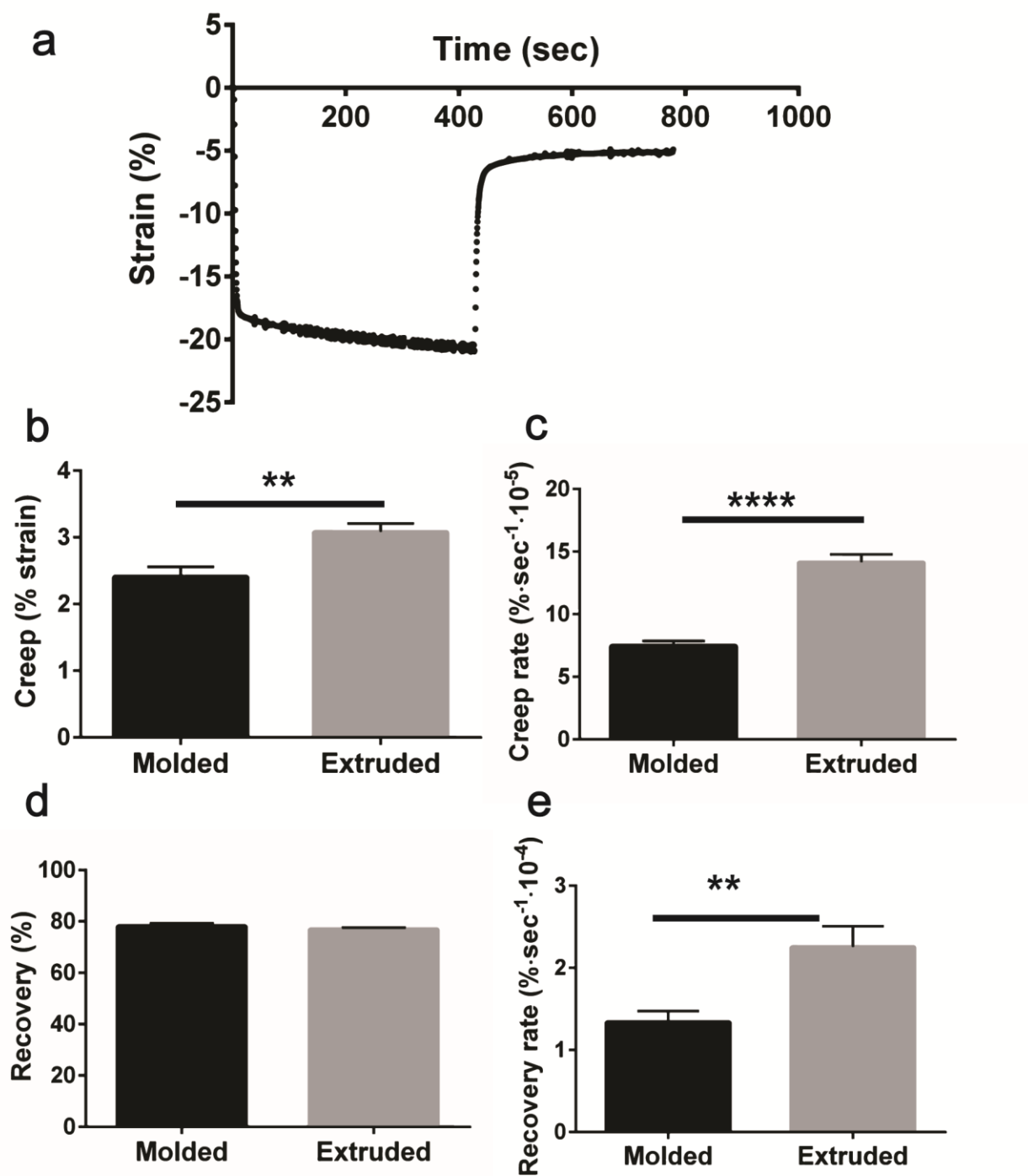
Figure 7. Printing affects rate and extent of time-dependent mechanical behavior. Printed and molded GelMA cylinders (15% GelMA, 0.25% LAP) were subjected to creep testing in hydrated unconfined compression. (a) Representative strain vs time data shown for creep + recovery testing of printed cylinders. (b) Creep extent data, obtained from exponential regression of creep portion ($p \leq 0.01$). (c) Creep rate data, obtained from exponential regression of creep portion (****$p \leq 0.0001$). (d) Recovery extent data, obtained from exponential regression of recovery portion. (e) Recovery rate data, obtained from exponential regression of recovery portion (**$p \leq 0.01$).**
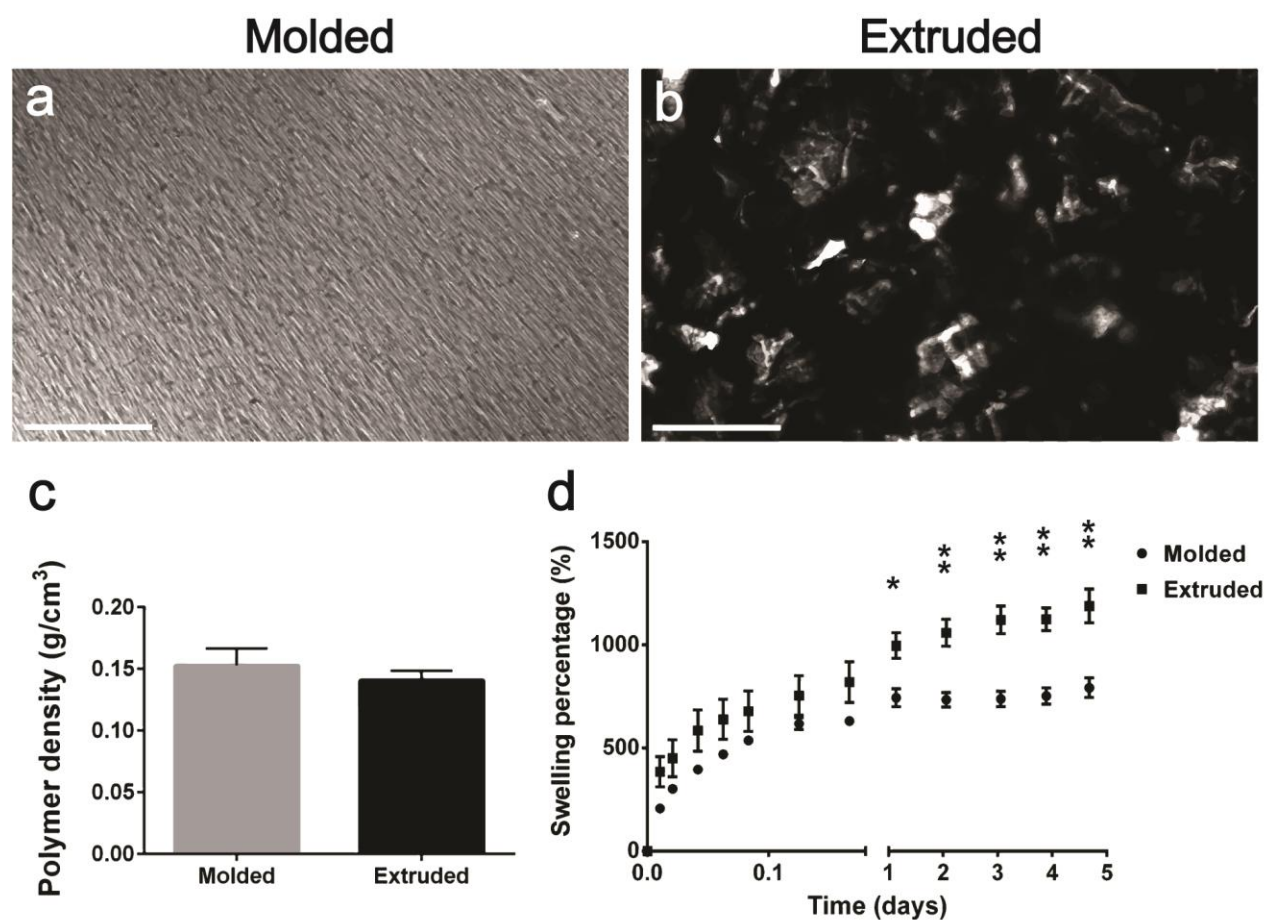
Figure 8. Printed and molded hydrogels exhibit different microstructures as well as swelling behavior.
Optical micrographs for molded (a) and printed (b) GelMA samples (15% GelMA, 0.25% LAP). Scale bars:
500 μm. (c) Polymer density of extruded and molded cylinders. No statistical difference between the two
groups. (d) Swelling percentage data (*p ≤ 0.05, **p ≤ 0.01) obtained from weighing printed and molded
GelMA cylinders (15% GelMA, 0.25% LAP) over time in immersion in PBS.

3.4. Discussion

Overall, our findings show that the bioprinting process results in hydrogels with unique

microstructures that differ from their molded counterparts prepared with the same polymer

solution and with the same dimensions, causing major changes in time-dependent mechanical

properties and swelling behavior.

The identification of optimal extrusion pressures and the observed increase in resolution

with printing speed and nozzle gauge are consistent with previous characterizations of extrusion-

based methods [88-90]. The impact of GelMA concentration on Young's modulus is also in agreement with previous studies performed with other photoinitiators [54]. However, the unexpected impact of GelMA concentration on resolution, very likely the result of increased flow resistance due to the concomitant rise of hydrogel viscosity with polymer concentration, reveals yet another mechanism at play in the determination of printing specifications. The fact that the extrusion process did not affect cell viability is in agreement with previous reports that allowing hydrogel solutions to undergo gelation prior to extrusion protects encapsulated cells from the detrimental effects of extrusion-induced shear forces [91].

More interesting is the finding that the extrusion process impacts the time-dependent mechanical behaviour of hydrogel constructs. The fact that swelling kinetics between molded and extruded hydrogels were different, despite similar densities, suggest that microstructural differences contribute to the observed differences. Indeed, the interstices present in the microstructure of the extruded construct constitute an interconnected network of space available to the surrounding medium, thereby increasing the rate and extent of fluid flow both into and out of the construct during loading and unloading. The differences in mechanical behavior of the extruded and molded constructs would be expected to be even greater after the hydrogels reached swelling equilibrium, which should be studied in future work. It is also possible that spatial differences in crosslinking existed because the first printed layers were exposed to the light source for longer periods of time than the last printed layers. However, because molded and extruded hydrogels did not show differences in elastic moduli, any spatial differences in crosslinking were likely too minor to affect mechanical properties. Finally, it is possible that lateral translation of the potentially unconstrained structural filaments with respect to each other may constitute another mechanism by which extrusion increases the rate and extent of creep.

However, our finding that the extent of recovery is identical in extruded and molded constructs suggests similar extents of permanent deformation. Clearly, further studies are warranted to thoroughly investigate the effects of the extrusion process on the microstructure and mechanical properties of hydrogels.

Time-dependent mechanical properties of extruded highly porous scaffolds have previously been evaluated, most notably with stress relaxation testing [92, 93]. These studies, however, solely assess the impact of intended scaffold porosity rather than the unintended impact of the extrusion process itself on the mechanical behaviour of constructs. Similarly, previous swelling studies performed on extruded constructs [39] overlook the impact of extrusion as they lack comparisons against molded counterparts. Interestingly, it was previously shown that the swelling behaviour of constructs fabricated with inkjet printing is not different from that of nonprinted hydrogels [94]. Given that inkjet printing dispenses liquid droplets that form a series of consolidated layers devoid of unintended discontinuities [95], these results serve to confirm our finding that interstices formed during extrusion are responsible for the observed differences in swelling behaviour. However, further studies are required to thoroughly characterize the microstructure of extruded and molded hydrogels.

This study did have several limitations. Firstly, the only biomaterial evaluated was gelatin methacrylate. Although this material is widely used in tissue engineering [54], the results may differ for other bioinks, including collagen [96], hyaluronic acid [97] and alginate [98], as well as other crosslinking methods such as physical or ionic crosslinking. In addition, this study only evaluated one composition of gelatin hydrogel in extruded and molded forms under just two mechanical testing scenarios. Future studies should include multiple time-dependent mechanical testing protocols for varying bioprinting parameters, namely extrusion speed and nozzle

diameter, as well as for constructs with different biomaterial formulations, all of which are likely to affect transient and equilibrium loading responses. Moreover, although our goal in this study was to compare the properties of extruded and molded hydrogels immediately after fabrication, mechanical characterization after the hydrogels reach swelling equilibrium also will be important for their intended functions. Nanoindentation studies may be more relevant tests to determine how encapsulated cells might respond to changes in mechanical behaviour [99]. Swelling studies should be conducted using osmotic solutions that more accurately recapitulate the intended application, as PBS has been shown to be a poor indicator of the high osmotic pressures found in many tissues *in vivo* [100]. Finally, we were not able to thoroughly characterize the microstructure of the hydrogel constructs, considering most methods of porosimetry require gel dehydration, which would affect the microstructure of the gels [87]. Future studies should be directed at characterizing differences in microstructure due to the extrusion process.

Concretely, the results of the study in Aim 1 establish a number of considerations for devising the cartilage template biofabrication strategy in Aim 2. First, since the filament-based printing process introduces interstices, creating a microstructure which promotes further swelling and time-dependent deformation, it's worth noting that printing resolution, which determines the size of extruded filaments and therefore the density of these interstices, also likely affects swelling and mechanical behavior in extruded hydrogels. Second, the excessive swelling observed with extruded hydrogels must somehow be mitigated to prevent unwanted scaffold deformation upon implantation. And finally, once the fabrication platform is established and constructs are generated, the characterization of these constructs must include time-dependent mechanical testing since we've now established that this property is sensitive to the 3D printing process.

4. Aim 2

4.1. Design implementation: criteria, constraints and envisioned strategy

In light of the proposed patient intervention strategy and the results from Aim 1, we've laid out a number of criteria and constraints to guide the development of the construct fabrication method:

- *Targeted defect types*: As previously discussed, given that most cases of bone trauma, cancer and infection target long bones [6, 9, 101] and that the endochondral ossification process is both endogenous to long bones during development and more widely studied in long bones in the context of native repair, templates will be targeted to critical size non-union defects involving long bones. In addition, it's important to note that non-union fractures require different intervention strategies depending on whether they're located at the midsection (diaphysis/metaphysis) or the distal/proximal ends (epiphysis/physis) because the two regions exhibit different compositional, geometric and mechanical properties [102]. Therefore, since over 70% of long bone fractures occur in the diaphysis or metaphysis region [103] and fractures along the midsection are often the gravest as they may break the skin and lead to infection [2], we've more specifically focused the target region of the proposed constructs to the midsection (diaphysis/metaphysis) of long bones.

- *Bulk size and shape:* As previously mentioned, critical-size defects, which are not capable of being repaired natively, have lengths of more than 2.5 to 3 times the diameter of the affected bone [3] and typically correspond to a volume range of 10-50 cm^3 [104]. The fabrication method must therefore accommodate any bulk shape and size

requirements within this volume range. This will be ensured by the scalability and shape conformation capabilities of additive manufacturing.

- *Surgical fixation*: Taking into account that the generated constructs would be surgically affixed to the site of injury using press fitting and compression plate fixation, both of which are established scaffold fixation methods [65, 105], the templates must withstand the press-fit strain needed for adequate fastening between the two separated bone segments. During press fitting, the prevention of implant sliding or loosening is ensured by the material and morphological properties at the implant surface as well as the strain experienced by the implant as a result of compression plate fixation [106]. Since hydrogels lack the material and frictional properties to ensure press fitting regardless of the applied strain, a reinforcing network is required for the proposed surgical fixation method. This reinforcing network must be strong enough to withstand the press fit strain as well as any additional strain which may be the result of micromotions typically observed in bone fixation plates. To that end, we require that the generated constructs not fracture before a compressive strain of 1%, which is sufficiently large to account for the applied press fit strain as well as fixation plate micromotions [107, 108].

- *Elastic modulus*: Considering the importance of mechanotransduction in the ossification process, we advance that the bulk elastic behavior of the fabricated constructs should be around that of native cartilage-like callous tissue in the initial stages of healing. The range of elastic moduli reported for both native hyaline cartilage and early soft callus tissue is 1-5 MPa [109, 110]. Within three weeks of healing, the elastic modulus of the callus region is estimated to increase to 50 MPa [111]. Since the hydrogel scaffolds to be fabricated will be reinforced with stiff networks in order to ensure the possibility of press

fitting, it is expected that their bulk elastic modulus will exceed the 5 MPa upper limit of native early soft callus tissue. However, this modulus must not be so great that stress shielding occurs, preventing the mechanotransduction of encapsulated cells. We postulate that an indicative point at which stress shielding becomes significant is the appearance of woven bone, which is the earliest and most disorganized type of bone tissue formed during endochondral ossification prior to trabecular bone formation [29, 30]. Accordingly, we've set the upper limit for the elastic modulus of the templates to the lowest reported values for the elastic modulus of woven bone, i.e. around 30 MPa [110, 112]. Thus, the bulk elastic modulus of the generated constructs must lie between 5 and 30 MPa.

- *Printing precision and consistency*: The use of additive manufacturing as part of the envisioned fabrication strategy is intended to ensure that complementary networks with varying architectures and dimensions are concurrently formed in each multi-material construct with accuracy over space and uniformity over time. This capability guarantees that different computer-generated architectures will lead to the formation of geometrically distinct experimental groups of constructs. Previous studies characterizing traditional 3D printing methods hold that geometric measurements with relative standard deviations smaller than 20% are indicative of adequate reproducibility [113]. Accordingly, to confirm that the employed additive manufacturing platform is able to attain the level of precision and consistency needed for adequate fidelity, we submit that the widths measured from any given strut element for a specific construct architecture must (1) not have a mean which deviates by more than 20% of the intended value (precision) and (2) not have a relative standard deviation of more than 20% (consistency).

- *Construct parameter modulation*: As previously discussed, we've established the capacity for parameter modulation as a requirement for the biofabrication platform in order to be able to conduct comprehensive studies with the generated constructs and to be able to tailor constructs on a case-by-case basis. Given that porosity constitutes the construct property which mediates both mechanical and fluid flow behavior, it would be reasonable to select it as the primary metric for tailorability. For comparison, the porosity of trabecular bone typically varies between 70% and 90%, which amounts to a porosity range of 20% [114]. Similarly, we require that the devised biofabrication method will be able to generate constructs a various porosities over a min-max range which exceeds 20%. As an added criterion, we also require that significant differences in mechanical and/or swelling behavior be observed depending on the porosity of the constructs generated.

- *Slow degrading material content:* As a crucial component of endochondral ossification, vascularization is another important consideration in the design of the biofabrication platform. Of note in the context of this design is the fact that the reinforcing network is expected to resorb in the span of weeks to months: the material thus amounts to volume inaccessible to vasculature. Indeed, bloods vessels would only be able to invade through the porous network and, to a lesser extent, through remodeled areas of the hydrogel (which resorbs faster than the slow degrading material). Accordingly, a maximal threshold must be set for slow degrading material content within the constructs. In native settings, the lowest porosities recorded for trabecular bone is 30% [115], which corresponds to a maximal bone content of 70%. Hence, we've set the maximal volumetric content of slow degrading material in the generated scaffolds to be 70%.

- *Swelling mitigation:* Based on previous animal implantation studies for bone defect repair, the swelling percentage of implanted hydrogels is acceptable if it is less than around 100%, which corresponds to 2-fold volumetric increase [116]. Moreover, in gelatin-based hydrogels with concentrations of less than 10%, dehydration causes over an 8-fold drop in volume [117]. Taking these two indicative values together, we submit that the mean equilibrium swelling percentage of dehydrated hydrogels within the generated constructs must not exceed 1500%, which corresponds to a 16-fold increase in volume.

Design Strategy: In order to retain the spatial control that 3D printing provides while barring the use of filament-based hydrogel extrusion, we've devised a fabrication technique which couples hybrid construct printing with hydrogel casting and sacrificial pore formation. More expressly, we envision printing a two-component porous construct using thermoplastic materials through melt extrusion. We then cast the hydrogel material (i.e. the cell-carrier component of the templates) into the porous network of the hybrid construct. Subsequently, we evacuate away one of the two thermoplastic components (i.e. the sacrificial network) of the construct, creating a secondary pore network for vascularization and nutrient supply. Thus, with this strategy, we are able to accurately shape the architectures of the stiff network, the hydrogel network and the pore network without having to riddle the hydrogel with interstices by extrusion.
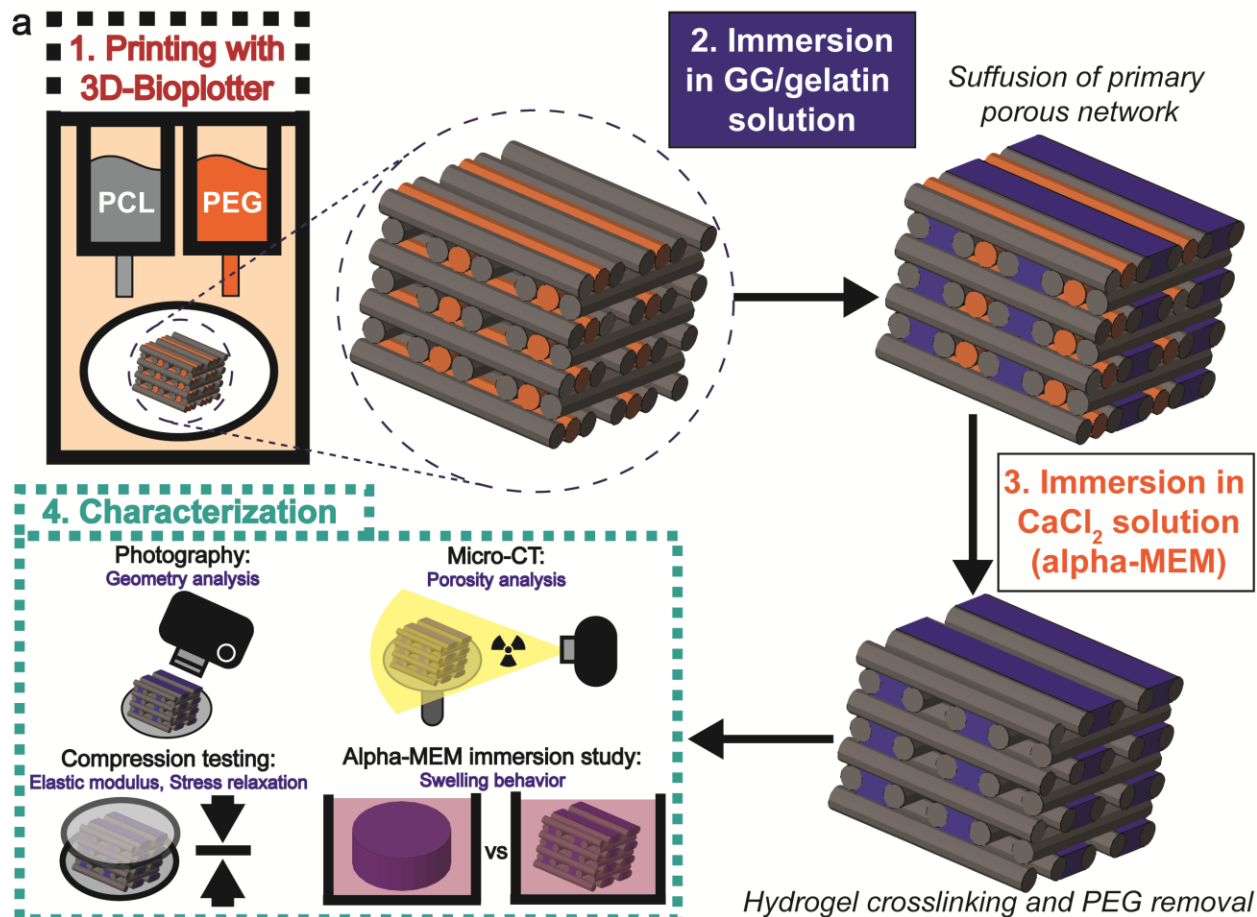
4.4. Experimental design, fabrication strategy and material selection

Material selections were made to accommodate for the devised fabrication strategy:

- *Reinforcing network*: Polycaprolactone (PCL) was chosen for the reinforcing network as it is widely used in scaffold fabrication, especially as a melt-extrusion polymer for accurate 3D printing [49, 118]. It is also water insoluble and slow-degrading, ensuring that it will remain present throughout the repair process upon implantation. At an average molecular weight of 14,000, PCL has a melting point of 65 °C.

- *Sacrificial network*: Since the PCL and sacrificial material create interweaving networks and must therefore be printed concurrently layer-by-layer, the sacrificial network should ideally be comprised of a thermoplastic material with a melting point similar to that of PCL to minimize print time and temperature fluctuations during melt extrusion. Yet the removal of the sacrificial material must also be relatively simple, non-toxic and rapid. Bearing these considerations in mind, we've selected poly(ethylene glycol) (PEG) for the sacrificial material as it is a stiff polymer extensively used in cell culture applications [119] and capable of being printed as a melt-extrusion polymer. At a molecular weight of 20,000, PEG has a melting point of 65 °C, equal to that of the selected PCL material. Importantly, it is water soluble and can therefore be dissolved away through simple immersion in aqueous media.

- *Hydrogel material*: Since the hydrogel must be cast within a micro-scale pore architecture and not printed, photocrosslinking is no longer an viable option: the hydrogel must be in a liquid, uncrosslinked form to be able to suffuse through the entire pore network. Only when complete suffusion occurs can this cell-carrying material be

crosslinked into a hydrogel. Accordingly, ionic crosslinking was chosen to be the hydrogel crosslinking method. To retain the cytocompatible and cell-adhesive properties of gelatin as seen in Aim 1, we've selected a mixture of gelatin and gellan gum (GG/gelatin) to be the basis for the hydrogel system. Indeed, while gelatin ensure cell-binding through its integrin motifs, gellan gum, another widely used biomaterial for cell encapsulation, ensures that crosslinking occurs in the presence of divalent cations [120], most notably Ca^{2+}, which is found in culture medium solutions such as Minimum Essential Medium Eagle – Alpha Modification (αMEM). In addition, the combinatorial use of gelatin and gellan gum has previously been shown to generate stable composite hydrogels [121]. Specifically, a composite formulation of 0.75% w/v gellan gum and 0.25% w/v gelatin generates a viscous liquid material at 37 °C which can be cast into the porous 3D printed constructs and subsequently crosslinked in a 0.2 g/L calcium chloride solution such as αMEM.

Figure 9a(1-3) illustrates the biofabrication strategy developed in accordance with the previously described strategy and the selected materials. Experimental groups were generated by varying the widths of the pore struts (0 mm, 0.5 mm and 1 mm) as well as the widths of the hydrogel struts (0.5 mm and 1 mm), as shown in Figure 9b-c. Generated constructs were subsequently charaterized by photography to assess geometry, by micro-computed tomography (micro-CT) imaging to verify that each intended fabrication step is achieved, by compression testing to evaluate mechanical behavior, and by swelling testing to assess fluid flow behavior into the constructs (Figure 9a(4)).

a

1. Printing with 3D-Bioplotter

PCL PEG

2. Immersion in GG/gelatin solution

Suffusion of primary porous network

3. Immersion in CaCl$_2$ solution (alpha-MEM)

Hydrogel crosslinking and PEG removal

4. Characterization

Photography:
Geometry analysis

Micro-CT:
Porosity analysis

Compression testing:
Elastic modulus, Stress relaxation

Alpha-MEM immersion study:
Swelling behavior

vs

b

		Pore Strut Width		
		1 mm	0.5 mm	0 mm (No pores)
Hydrogel Strut Width	1 mm	1P/1HG (**25%**)	0.5P/1HG (**14%**)	0P/1HG (**0%**)
	0.5 mm	1P/0.5HG (**29%**)		

c

0P/1HG

1 mm

0.5 mm

1P/1HG

1 mm 1 mm

0.5 mm

0.5P/1HG

1 mm 0.5 mm

0.5 mm
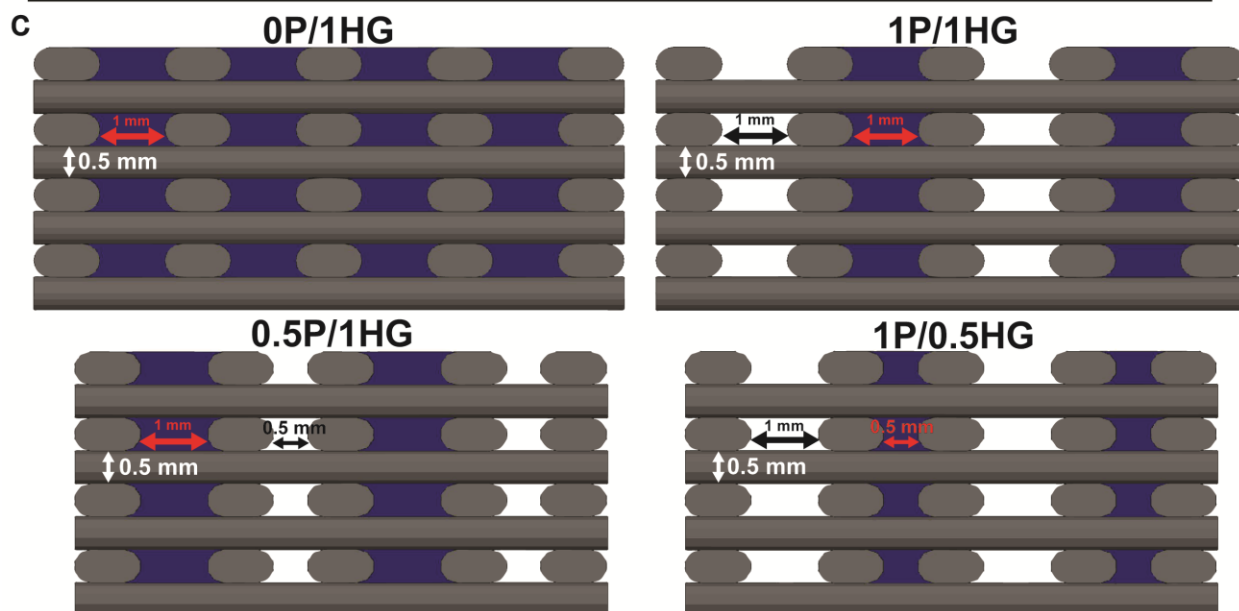
1P/0.5HG

1 mm 0.5 mm

0.5 mm

Figure 9. Cartilage precursor template preparation process. (a) A porous hybrid construct is printed by interweaving crosshatch networks of PCL (gray) and PEG (orange) in a repeating PCL strut-pore channel-PCL strut-PEG strut pattern and immersed in a non-crosslinked, composite GG/gelatin solution (blue) to fill the primary porous network. The construct is subsequently immersed in culture media containing Ca2+ in order to crosslink the solution into a hydrogel and dissolve away the PEG network, creating a secondary porous network. Characterization of final, sectioned constructs included geometry analysis by photography, porosity analysis using micro-CT scans, mechanical testing and a swelling study. (b) Established nomenclature of construct experimental groups as classified by hydrogel channel thickness and pore channel thickness. Percentages indicated correspond to construct porosities. (c) Computer models of all four experimental groups. Generated constructs consisted of 10 layers, each with a height of 0.5 mm, and had bulk dimensions of 5 mm x 5 mm x 5 mm. PCL struts had widths of 1 mm. Both the widths of the primary pore channels to be filled with hydrogel material and the PEG struts to be dissolved away forming secondary pore channels were varied to values of 0.5 mm and 1 mm.

4.5. Methods

4.5.1. 3D printing

Using an EnvisionTEC 3D-Bioplotter®, poly(ethylene glycol) (PEG; average Mn 20,000; Sigma) heated to 80°C and polycaprolactone (PCL; average Mn 14,000; Sigma) heated to 90°C were melt-extruded into porous hybrid constructs with a crosshatch architecture and a repeating PCL strut-pore channel-PCL strut-PEG strut pattern. The extrusion process was performed on matte paper and both PCL and PEG printing heads were fitted with stainless steel 24G needles (300 μm inner diameter; Sigma). Printing speed was set to 3 mm/sec for the PCL head and 2 mm/sec for the PEG head. Extruded templates consisted of 10 layers, with each layer having a height of 0.5 mm. Both the widths of the primary pore channels and those of the PEG struts were varied to values of 0.5 mm and 1 mm by altering the dimensions of the computer generated 3D models imported into the 3D-Bioplotter software. The printed templates were subsequently sectioned into samples of size 5 mm x 5 mm x 5 mm using a surgical scalpel.

4.5.2. Hydrogel suffusion and PEG removal

A composite (GG/gelatin) solution of 0.75% w/v gellan gum (GG) and 0.25% w/v gelatin was prepared by dissolving Gelzan™ CM (Sigma) and Type A, 300 bloom, porcine skin gelatin

(Sigma) powders in deionized water at 37°C under stirring. Sectioned samples were immersed in the prepared composite solution, which was subsequently allowed to cool to room temperature. After 15 minutes, samples were removed from the composite solution and immersed in Minimum Essential Medium Eagle – Alpha Modification (αMEM), which contains 0.2 g/L calcium chloride, for 2 hours at 37°C in a stirring water bath to ensure PEG dissolution and crosslinking of the composite solution into a hydrogel.

4.5.2. Construct imaging and width analysis

Top and isometric photographs of samples from each experimental group both after printing and after sectioning were taken using a Canon PowerShot G11 camera. The widths of the PCL struts, PEG struts and hydrogel channels were obtained using the scaling and measuring functions in ImageJ through manual endpoint selection over multiple struts and channels.

4.5.3. Micro-computed tomography

Construct architecture was analyzed by micro-computed tomography using a calibrated desktop micro-CT scanner (SkyScan 1272, Belgium) at a voltage of 50 kV and a current of 200 μA. Four sectioned 1P/1HG constructs were scanned at an *xyz* resolution of 15 μm and an exposure time of 160 ms: one immediately after extrusion, a second after αMEM immersion over 2 hours, a third after immersion in a composite GG/G solution cooled to room temperature for physical gelation, and a fourth after immersion in a composite GG/G solution cooled to room temperature and subsequently in αMEM for 2 hours. Obtained isotropic slice data were reconstructed into 2D *xy* slice images, which were in turn compiled and analyzed to render 3D *xyz* images. Samples were reconstructed using a region of interest (ROI) with approximately 200 slices. Threshold levels were set to eliminate image noise and distinguish combined PCL, PEG and hydrogel material from pore regions. Porosities were determined using the software by

selecting regions of interest which, in the *xy* plane, correspond to unit pattern elements of the constructs' repeating architecture.

4.5.4. Mechanical testing

Final constructs from all experimental groups were placed on the compression platens of an Instron 4411 Materials Testing Machine (Instron Ltd, High Wycombe, England) in an unconfined setup, immersed in PBS, and preloaded with a compressive stress of 40 kPa prior to each test. The performed stress relaxation test consists of an initial uniaxial compression portion to a strain of 5% at a rate of 0.5% per second, followed by dwelling at that strain for 2 minutes (stress relaxation portion). Linear regression was performed on the obtained stress-strain data over the initial 1% of strain to obtain the slope of the initial linear portion of the stress-strain curve (Young's modulus). Exponential fitting of the stress relaxation portion of the data was performed using equation 4, where σ represents stress. a_{relax} corresponds to the change in stress caused by relaxation while b_{relax} corresponds to the equilibrium stress value reached over time. τ is a time constant that corresponds to the amount of time it takes for the stress to reach approximately 37% of its final value (1/e).

$$\sigma = a_{relax} \, exp\left(-\frac{t}{\tau}\right) + b_{relax} \qquad (4)$$

From the fitting, time-dependent mechanical behavior was quantified using the total change in stress during relaxation ($-a_{relax}$), the total change in stress as a percentage of the initial stress prior to relaxation ($a_{relax}/(a_{relax}+b_{relax})$x100%) and the average stress rate, which corresponds to the average rate of change of stress over the initial 99% of stress relaxation.

4.5.5. Swelling test

A swelling kinetics study was performed to assess differences in hydrogel swelling in the presence of the PCL network and in unconstrained conditions. Fully prepared 0P/1HG constructs

were dried over a period of 1 week. Given the known initial weight concentration of the

GG/gelatin hydrogel and assuming the measured decrease in weight during drying corresponds

to the initial water weight of the GG/gelatin hydrogel material contained within the constructs,

plain weight-matched GG/gelatin hydrogels were also prepared and dried over a period of 1

week. Both 0P/1HG constructs and plain hydrogel samples were subsequently immersed in 10

mL αMEM and weighed at multiple time points over 7 days of swelling. Swelling percentage

was calculated using equation (5), where M_t corresponds to the hydrogel mass at time t and M_0

corresponds to the initial weight of the dried GG/gelatin polymer prior to immersion in PBS.

$$Swelling\ percentage = \frac{M_t - M_0}{M_0} \times 100\% \quad (5)$$

4.5.6. Statistics

One-way ANOVA with post-hoc Tukey analysis was performed to determine statistical

significance between groups in the strut/channel width data and the mechanical testing data. A

two-tailed t-test with Holm-Sidak correction for multiple comparisons was performed on the

swelling percentage data. All graphs are shown as mean ± SEM and the line width data is shown

as mean ± S.D., with n=8 for the strut/channel width data, n=1 for the porosity data from micro-

CT imaging, n=6 for the mechanical testing data and n=7 for the swelling data. All graphs were

plotted using GraphPad Prism 6 software. A *p*-value of less than 0.05 was considered statistically

significant.

4.6. Results

4.6.1. Construct geometry assessment

Immediately after the 3D printing of porous hybrid constructs from all four experimental groups, geometric analysis was performed by photography, as seen in Figure 10, to assess printing fidelity and consistency. Recorded measurements, shown in Table 2, include PCL strut widths, PEG strut widths and the widths of primary porous network channels to be filled with hydrogel. Overall, measurements remained close to intended values, with means not straying from target by more than 0.16 mm. Given the low variation in values for measurements from each group, which is indicative of high consistency, the observed differences between intended and targeted values are most likely the result of offsets in the width of elemental filaments between the computer models and actual extrusions.

4.6.2. Porosity assessment by micro-CT

To ensure that the construct preparation steps occurred as anticipated, a single 1P/1HG print was sectioned into four constructs, one of which remained unchanged while the other three were subjected to different steps of the preparation process, including (1) immersion in aqueous media (αMEM) to verify complete PEG dissolution, (2) immersion in a GG/gelatin solution and crosslinking in αMEM to ensure complete hydrogel suffusion, and (3) immersion in a GG/gelatin solution followed by immersion in αMEM to confirm final construct formation. Each construct was scanned using micro-CT and, since the described steps amount to material additions and removals with associated volumetric changes, the success of each preparation step was evaluated by comparing the porosity measurement from each construct against the corresponding expected value. Overall, measured porosity percentages did not stray by more than 11% from targeted values, indicating that both PEG dissolution and hydrogel suffusion were complete and

successful when carried out both separately and sequentially, though more extensive studies are required to confirm this finding.

0P/1HG
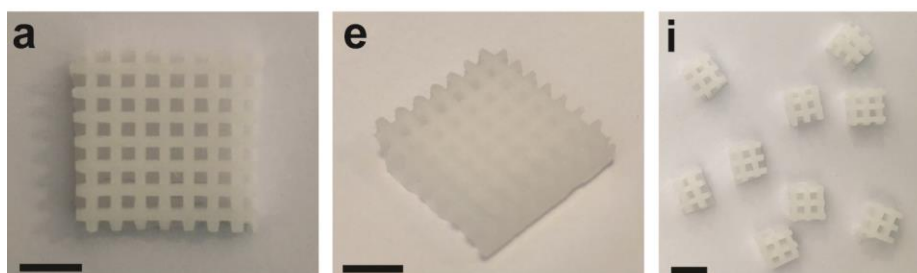
1P/1HG
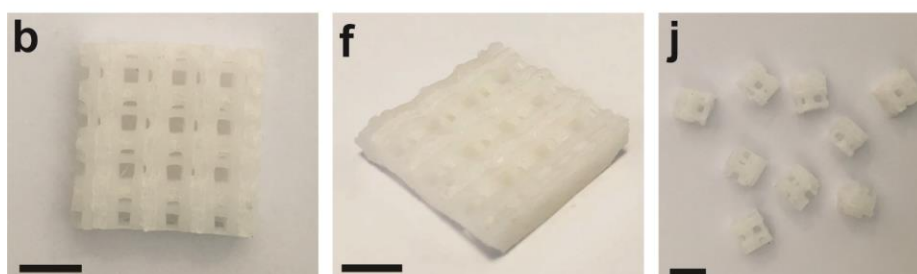
0.5P/1HG
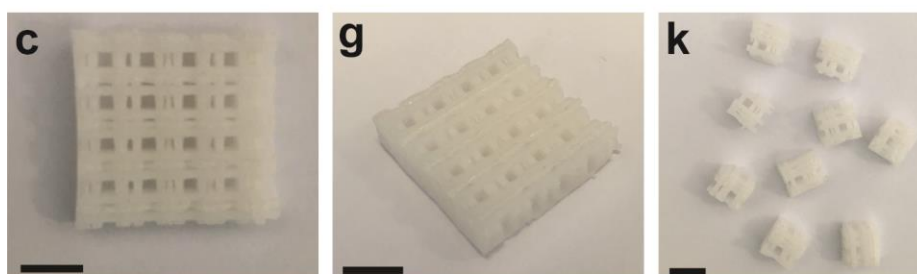
1P/0.5HG
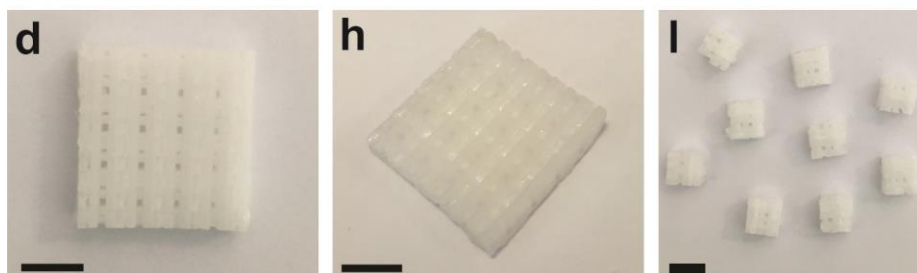
Figure 10. Photographic evaluation of constructs from all experimental groups immediately after printing from top (a-d) and isometric views (e-h) as well as after sectioning into individual samples (i-l). All scale bars: 0.5 mm.

Table 2: Widths of PCL struts, PEG struts and hydrogel channels for all experimental groups calculated from obtained images. Data shown as mean ± S.D.

Group	PCL struts	PEG struts	Hydrogel channels
0P/1HG	0.928 (± 0.0417)		1.064 (±0.0435)
1P/1HG	0.930 (±0.127)	1.158 (±0.0989)	1.093 (±0.0738)
0.5P/1HG	0.871 (±0.105)	0.646 (±0.0581)	1.034 (±0.143)
1P/0.5HG	0.857 (±0.101)	1.024 (±0.0727)	0.542 (±0.120)

Intended width of 1 mm

Intended width of 0.5 mm
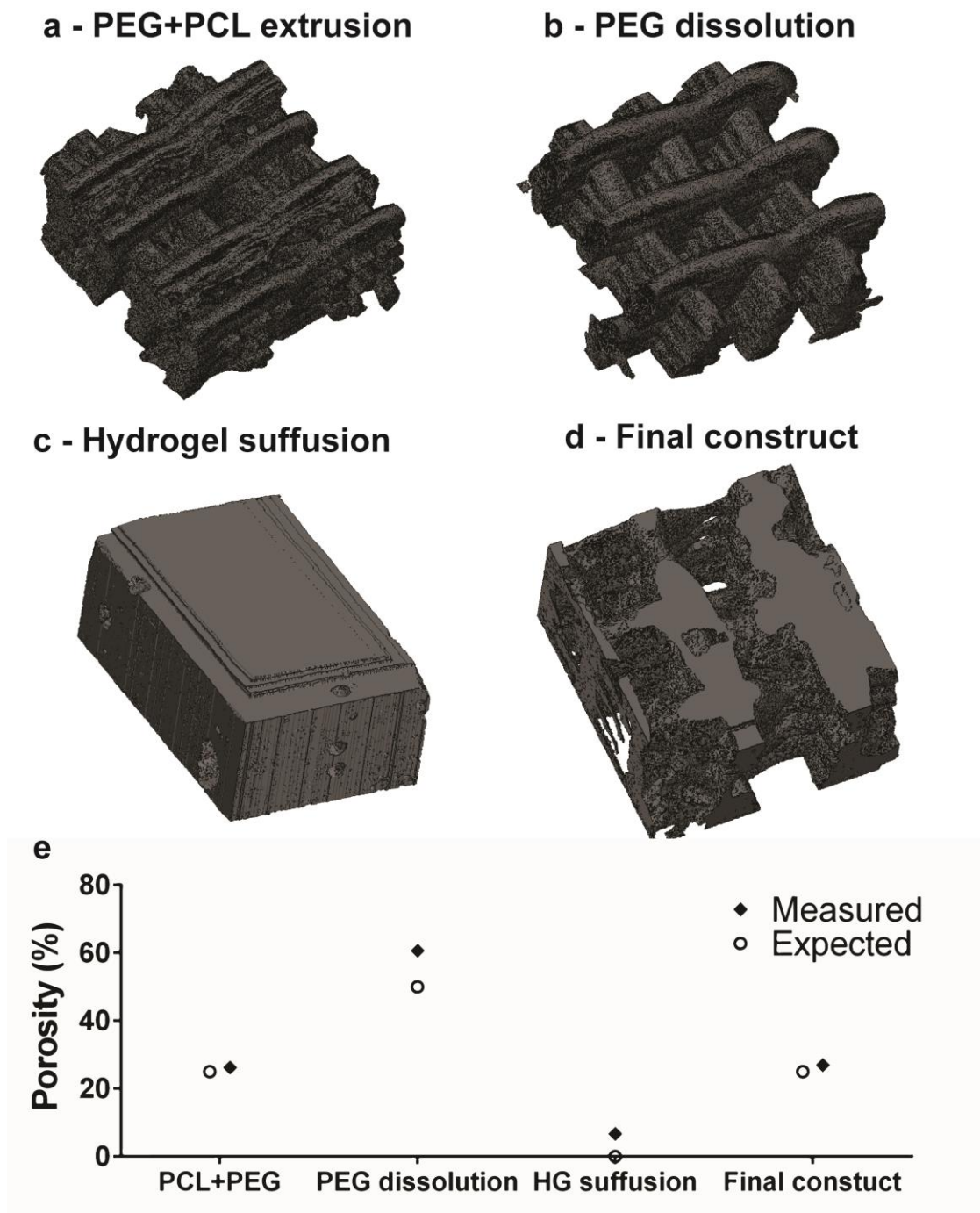
Figure 11. 3D images rendered from micro-CT scanning of 1P/1HG samples at different stages of preparation confirm complete hydrogel suffusion into the primary porous network as well as the dissolution of the sacrificial PEG network, leading to the formation of a secondary porous network. (a) Scan of 1P/1HG construct immediately after extrusion. (b) Scan of 1P/1HG construct immersed in culture media after extrusion. (c) Scan of 1P/1HG construct immersed in hydrogel solution after extrusion. (d) Scan of 1P/1HG construct immersed in hydrogel solution and subsequently in culture media. (e) Porosity values of the 1P/1HG construct at each stage of preparation as expected from designs and as measured from generated micro-CT scans.

4.6.3. Mechanical properties

To evaluate both bulk elastic and time-dependent mechanical properties of the generated templates, final constructs from all four experimental groups were subjected to stress relaxation testing under unconfined hydrated testing, whereby strain was linearly increased to 5% and held constant for 2 minutes (Figure 12a). No failure was observed in any of the constructs during and after testing. Elastic modulus measurements, calculated from the stress and strain data obtained during the linear increase in strain, were quite similar across all groups, as shown in Figure 12b, with a global average of 26.3 (±1.14) MPa.

Time-dependent mechanical behavior was also quantified using exponential regressions of the relaxation portion of the stress vs time data. Specifically, the extent of stress change both alone (Figure 12c) and as a percentage of stress immediately prior to relaxation (Figure 12e), the time constant τ indicative of the time scale of relaxation (Figure 12d), and the average rate of stress change over the initial 99% of relaxation (Figure 12f) were calculated. Though no significant differences were found across groups for τ, values for the 1P/0.5HG group were markedly and consistently higher than values for the 0.5P/1HG group across the three remaining metrics. In addition, we note a trend of differences isolating the 0P/1HG group from other groups. Indeed, the 0P/1HG group had a greater absolute change in stress during relaxation compared to the 1P/1HG and 0.5P/1HG groups as well as a lower change in stress as a percentage of initial value during relaxation compared to the 1P/0.5HG group.
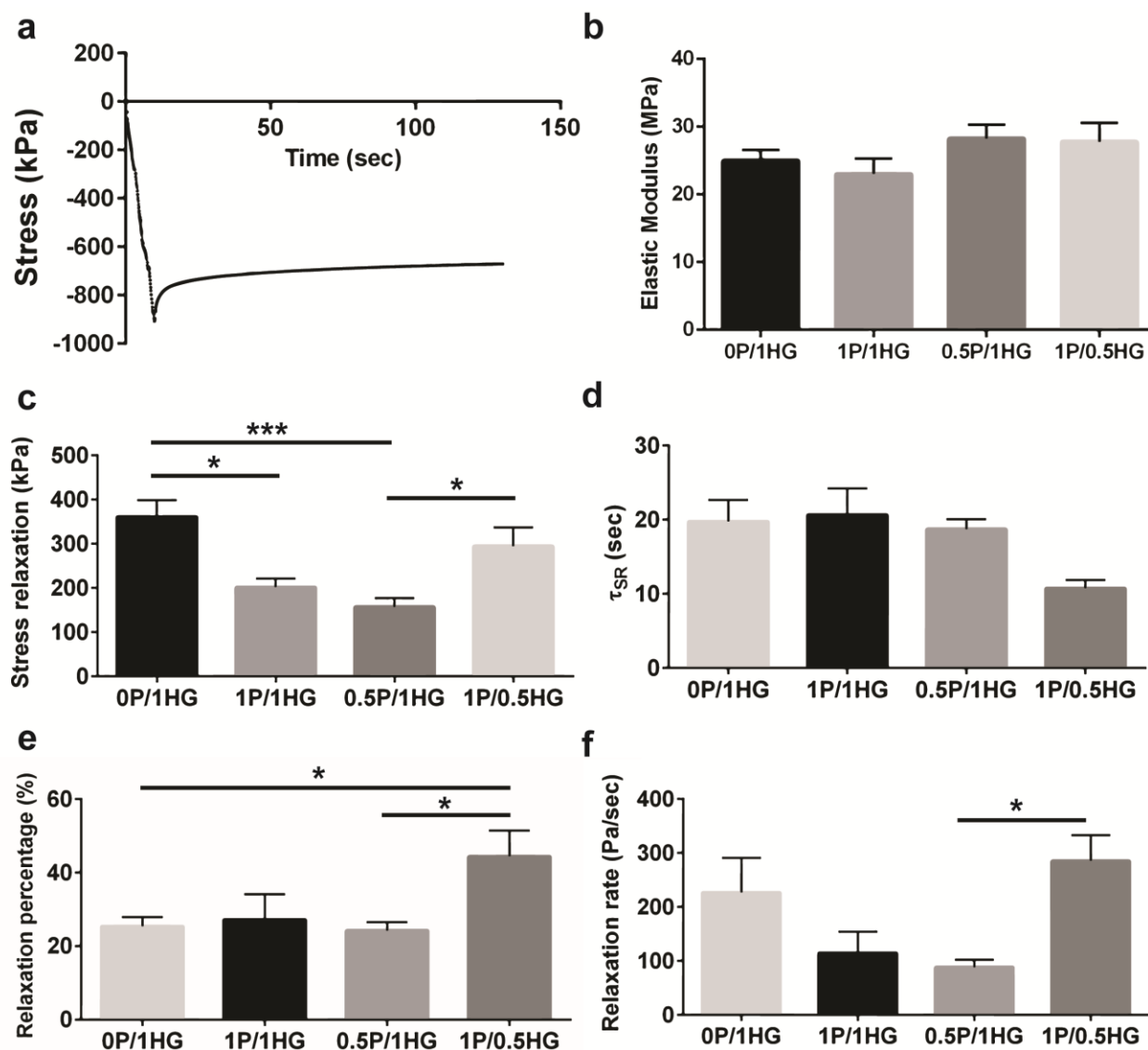
Figure 12. Interplay between pore and hydrogel geometries alters the time-dependent mechanical properties of prepared constructs. (a) Representative stress vs time curve obtained from stress relaxation testing protocol. (b) Young's moduli of constructs from all experimental groups. Total stress relaxation (c), τ value of stress relaxation (d), total stress relaxation as a percentage of initial stress (c) and average stress relaxation rate (d) in constructs from all experimental groups as determined from exponential regressions of the stress relaxation portion of mechanical testing (*p ≤ 0.01, ***p ≤ 0.001, one way ANOVA and Tukey post hoc analysis).

4.6.4. Effect of stiff network on hydrogel swelling behavior

To probe the impact of the reinforcing stiff PCL network in the rate and extent of fluid flow into the GG/gelatin hydrogels, a swelling study was performed with dried 0P/1HG constructs and dried weight-matched hydrogel control samples (without a reinforcing stiff network) over the course of 7 days. Within a half hour of swelling, significant differences appear between the two groups and persist until day 4 with the control group exhibiting considerably greater swelling percentages, which confirms that hydrogel swelling is indeed constrained by a reinforcing stiff network. Interestingly, at day 7, though the mean swelling percentage of the control group was over two times greater than that of the 0P/1HG group, no significant difference was found between the two groups.

Figure 13. Hydrogels in 0P/1HG constructs and weight-matched plain hydrogel control exhibit different swelling behavior. Swelling percentage data (*p ≤ 0.05, **p ≤ 0.01, ***p ≤ 0.001) obtained from weighing hydrogels immersed in culture medium over time.
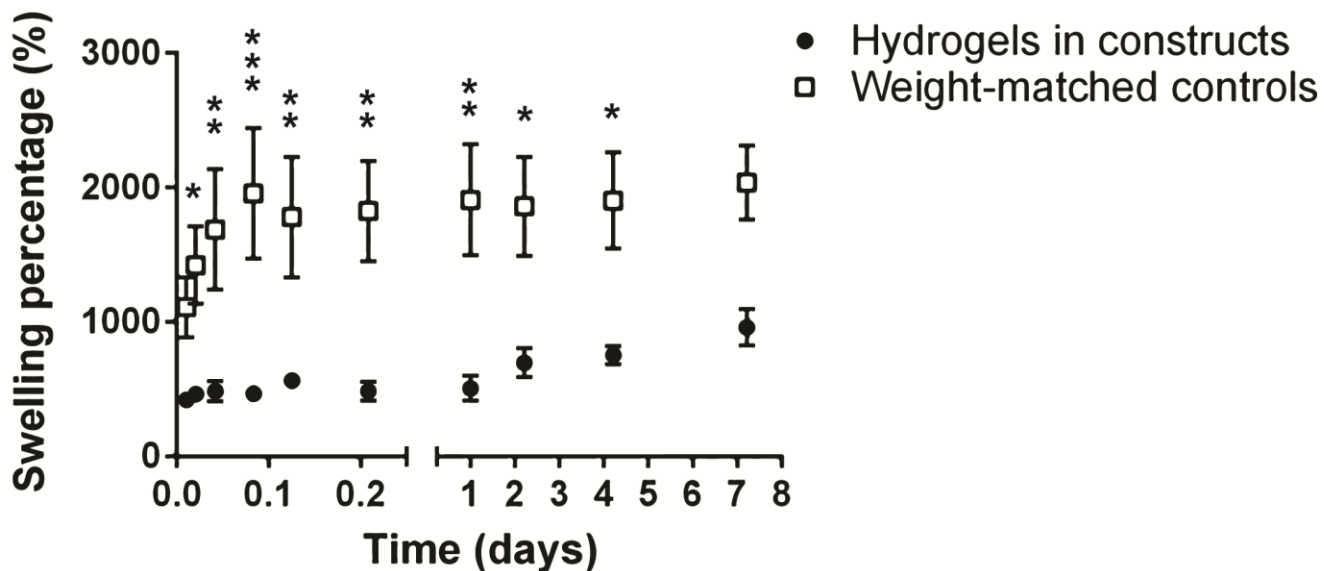
4.7. Discussion

Characterization results for the generated constructs establish the proposed biofabrication strategy as a viable method of producing tailorable constructs for bone defect repair through endochondral ossification. Indeed, the developed fabrication strategy is capable of generating templates with great spatial resolution as well as tunable architectural and mechanical properties whilst still minimizing unwanted swelling deformation. In addition, the decision to cast the hydrogel material instead of extruding it will very likely be of benefit to encapsulated cells as they will not be subjected to the damaging shear stresses experienced during extrusion [122]. Nevertheless, more extensive studies remain to be made to confirm findings and optimize the platform. For instance, though the printing process was shown to be fairly consistent as evidenced by the minimal variation in geometric measurements across replicates, some improvements could be made with printing fidelity by further harmonizing the widths of individual extrusion filaments with those of corresponding computer generated models. Moreover, additional replicates across all experimental groups are certainly required to confirm the obtained micro-CT results according to which each step of the fabrication process was successful.

Delving into the mechanical properties of the constructs, it is reasonable to assume that, discounting volumetric composition, since the compressive modulus of polycaprolactone, which is recorded to be around 40 MPa [123], is markedly higher than that of the hydrogel material, which would be in the order of 0.1 MPa as supported by findings from Aim 1, polycaprolactone would be the primary determinant of elastic modulus in these constructs. It therefore stands to reason that the experimental groups with the highest PCL content, namely 0.5P/1HG and 1P/0.5HG, would exhibit higher moduli compared to groups with lower PCL content, namely

0P/1HG and 1P/1HG. Yet surprisingly, though the means of the high PCL content groups were to be sure higher than those of the low PCL content groups, there was no significant difference between any of the groups. Although the presence of hydrogel material in the constructs might account for this, a more likely explanation can be found in the dimensions of the tested constructs, which were 5 mm x 5 mm x 5 mm. It is possible that, at this size, the PCL networks might have buckled under compression in such a way that the differences in PCL content between groups were not found to have had a significant impact on elastic modulus. This is supported by findings that properties such as elastic modulus are dependent on size for both PCL and other materials [124, 125]. Further compression testing with constructs of greater size would be required to verify this hypothesis.

Contrary to the uniformity observed across experimental groups vis-à-vis elastic behavior, time-dependent mechanical behavior exhibited significant variability across groups for multiple metrics. The most crucial indicator in the elucidation of the primary mechanism behind stress relaxation in these constructs is the finding that differences were most consistently seen between the 0.5P/1HG and 1P/0.5HG groups. From a structural standpoint, though both groups have the same PCL content (57% by volume), they are the two most dissimilar groups in terms of the ratio of porosity to hydrogel content. Indeed, while the 0.5P/1HG group has a porosity of 14% and a volumetric hydrogel content of 29%, leading to a porosity-to-hydrogel content ratio of 0.5, the 1P/0.5HG group has a porosity of 29% and a volumetric hydrogel content of 14%, leading to a porosity-to-hydrogel content ratio of 2. For comparison, the porosity-to-hydrogel content ratio of the 1P/1HG group is 1. And since both the extent and rate of stress relaxation is greater in the 1P/0.5HG group compared to the 0.5P/1HG group, we can surmise that the likely mechanism of stress relaxation in the constructs during compression is the squeezing of hydrogel

material into pore spaces which alleviates internal stresses. Since there is the most amount of

pore space with respect to hydrogel material in the 1P/0.5HG group, it is therefore quite tenable

that hydrogel material was displaced faster and to a greater extent into the pore network, leading

to greater stress relaxation and an increased relaxation rate. Conversely, since there is the least

amount of pore space with respect to hydrogel material in the 0.5P/1HG group, hydrogel material

was squeezed slower and to a lesser extent into the pore network, leading to lower stress

relaxation and a decreased relaxation rate. Another group with marked differences in time-

dependent mechanical behaviour compared to others is the 0P/1HG group. This observation,

compounded with the fact that there is no porosity in the 0P/1HG group, suggests that another

mechanism is at play during relaxation under compression in this group. Looking closer, the

finding that the 0P/1HG group had the greatest absolute change in stress yet the second lowest

change in stress as a percentage of initial value indicates that great stresses were accumulated

prior to relaxation during the linear increase in strain. This is most probably because there were

no stress-alleviating pores into which hydrogel material could have been forced into. The

ensuing hypothesis is therefore that stress relaxation was achieved in the 0P/1HG constructs

through the simple displacement of hydrogel material outside of the construct boundaries. We

note that the proposed conjecture for stress alleviation through squeeze deformation has been

explored in previous studies, examples of which include mechanical characterizations of

hydrogels for cartilage and nucleus pulposus engineering [126, 127], lending additional credence

to our hypothesis.

Finally, the swelling study results serve to confirm another method by which swelling

deformation may be constrained using the developed biofabrication strategy: the presence of a

reinforcing stiff network reduces the rate and extent of fluid flow into hydrogels by acting as a

physical barrier to increasing hydrogel volume. Interestingly, as previously observed, no significant difference was found at day 7 between the swelling percentages of the 0P/1HG and control groups, though we did note that the mean swelling percentage of the control group was over two times greater than that of the 0P/1HG group. A possible explanation for this is that between days 4 and 7, the hydrogel material fully enveloped the stiff network in the 0P/1HG constructs, thereby eliminating the ensuing effectiveness of the stiff network at constraining swelling.

Overall, a follow-up comprehensive investigation is required to validate the interesting findings and conjectures regarding the fabricated constructs, especially with respect to mechanical and swelling behavior, given the limitations of the conducted study. Firstly, additional tests are required to probe the veracity of the advanced hypotheses, including testing with constructs of greater size, creep testing to confirm stress relaxation findings, and visualization of hydrogel squeeze/swell-based deformation through optical microscopy or 3D imaging methods. The study could also benefit from complementing mathematical models (ex: a finite element analysis of the stress relaxation tests) which could account for key findings. Finally, cell studies are needed to investigate whether cell encapsulation alters any construct properties. Once such an extensive study is completed, viability, tissue differentiation and pre-clinical animal implantation studies are warranted to fully confirm product feasibility and to investigate how parameter modulation impacts the efficiency of the constructs with respect to bone defect repair. Given that the porosity-to-hydrogel content ratio is lowest for the 0.5P/1HG group and that hypoxia has been widely shown to promote chondrogenesis [128, 129], we surmise *a priori* that the 0.5P/1HG group will generate tissue most similar to cartilage and will therefore perform better upon implantation.

5. Evaluation of proposed strategy and conclusions

5.1. Criteria/constraint satisfaction

At the conclusion of the study, we gauged the success or failure of the developed biofabrication strategy with respect to each previously established criteria and constraint:

- *Bulk size and shape for targeted defect types:* Though construct characterization was performed at the spatial scale of unit elements of the PCL, hydrogel and pore network architectures, the use of additive manufacturing and the structural integrity that the stiff network provides ensure that the generated constructs may be scaled up and shaped to conform to any non-union defect along the mid-section of long bones.

- *Surgical fixation:* It was found that during mechanical testing, none of the constructs fractured at strains of up to 5%, which exceeds the 1% limit criteria previously set and confirms that the generated templates will not fail during implantation upon press fitting and plate fixation.

- *Elastic modulus*: With a global mean of 26.3 ($\pm$1.14) MPa and fairly uniform measurements across replicates and groups, the generated constructs are acceptably within the 5-30 MPa range established to prevent stress shielding and ensure mechanotransduction while adequately supporting press fitting.

- *Printing precision and consistency*: The greatest deviation in width mean from target value was found to be 29% (9% greater than the set criteria value) while the largest relative standard deviation for any given group of measurements was reported to be 22% (2% greater than the set criteria value). The employed additive manufacturing platform therefore narrowly misses both the targeted precision and

consistency levels required to produce either distinct or identical multi-material

constructs as neede. Thus, as previously discussed, printing fidelity should be

further improved by harmonizing the widths of individual extrusion filaments

with those of corresponding computer generated models. In addition, minor

improvements stand to be made in terms of ensuring geometric uniformity across

multiple iterations of the same printing task. This can be accomplished by further

standardizing environmental conditions, which include ambient temperature, air

convection and the amount of loaded material within extrusion cartridges, across

all prints.

- *Construct parameter modulation:* By successfully modulating pore and hydrogel

  strut widths in the construct architecture, the developed fabrication strategy was

  able to generate constructs with a variety of porosities exceeding the set minimal

  range of 20% and with marked differences in time-dependent mechanical

  behavior, all of which confirms the tailorability of generated constructs through

  parameter modulation.

- *Slow degrading material content:* The maximal volumetric PCL content in the

  fabricated scaffolds, which was 57%, is also acceptably under the established

  threshold of 70%, which lends support to the prediction that the generated

  templates will support adequate vascularization.

- *Swelling mitigation:* In addition to the reduction in swelling achieved through the

  successful elimination of hydrogel extrusion from the fabrication process, the

  incorporation of a stiff network also participated in further constraining swelling.

  Indeed, the recorded swelling percentage remained well under 1500% after 1

week of swelling. These findings lend credence to the expectation that

deformation due to swelling will be minimized.

Thus, overall, the developed fabrication strategy met nearly all of the previously established

criteria and constraints, though we note that more rigorous standards must be implemented

during the previously proposed comprehensive follow-up investigation in order to validate

predictions with respect to structural integrity for fixation, mechanotransduction, parameter

modulation, hydrogel deformation and vascularization.

5.2. Decision matrix against alternative bone defect repair strategies

The advanced approach to bone defect repair was also evaluated against previously

discussed alternative strategies in the clinical and tissue engineering realms, namely previous

techniques aiming to mimic endochondral ossification without the use of 3D printing, non-

resorbable implants such as ceramics and metals, resorbable scaffolds for direct osteogenesis,

autologous grafts, and allogeneic grafts. This assessment was performed based on a number of

points, each scored on a scale of 1 (most inadequate) to 5 (most ideal):

A primary set of considerations, which were each assigned the highest weight of 3 in the

evaluation process, relate to the pure feasibility of developing a medical product targeting the

bone defect market. In essence, these considerations constitute prerequisites to developing a safe

and efficacious implantable construct. Specifically, they include (1) the possibility of grave

complications (such as immune rejection, toxicity and loosening), (2) load bearing function upon

implantation, (3) successful fixation at the time of implantation, and (4) eventual

osseointegration (as a result of vascularization, endochondral ossification, osteoinduction or

osteoconduction). For the prevention of complications, lower scores were assigned to the gold standard methods of autologous and allogeneic grafting since their numerous shortcomings are what are currently fueling the investigation into alternative strategies. Load bearing function upon implantation was deemed best for non-degradable implants due to the strong mechanical properties of metals and ceramics, and worst for hydrogel-based tissue engineering approaches which require additional fixation methods to withstand native loads. Similarly, successful fixation was considered to be most ideal with non-resorbable implants since metals and ceramics constitute sturdier substrates for existing fixation methods. Finally, osseointegration was estimated to be best with endochondral ossification-based methods since mimicking the native repair process would generate the most native-like and integrated bone tissue.

The next set of considerations, each assigned a weight of 2, relate to the maximization of implant success across the most number of patients. Specifically, these considerations include (5) widespread availability for mass production, (6) tailorability of bulk size, shape, microscale architecture and mechanical properties, and (7) the implant lifespan, which determines the frequency of follow-up interventions (each of which has an associated risk). The greatest score for availability was assigned to non-degradable implants, which are made of entirely synthetic and widely accessible materials, while the lowest score was accorded to autografts due to the shortage of donor bone tissue sites within each individual. As for implant lifespan, the highest scores were accorded to strategies which target complete regeneration and therefore eventually do away with foreign materials in the body either through surgical removal or native resorption.

The last consideration, which is assigned a weight of 1 and pertains to convenience and quality of life for patients, corresponds to the total duration of the first intervention. Non-resorbable implants were rated highest for intervention duration since metal and ceramic

implants can be made ready for implantation as soon as bone defect cases present. Conversely, tissue engineering strategies were rated lower since they require a preliminary intervention to immobilize the defect area while constructs are fabricated and cultured to maturation before implantation can occur.

The results of this comprehensive comparison can be seen in the decision matrix in Table 3. Overall, we note that our proposed strategy involving 3D printing, hydrogel casting and sacrificial pore formation brings the formerly lagging endochondral ossification approach to the forefront, making it a viable strategy capable of competing with alternative potential solutions and claiming a considerable portion of the bone defect market share.

Table 3: Decision matrix between proposed approach and alternative solutions.

	Assigned weight	Proposed approach	Previous ossification techniques	Metal and ceramic implants	Bioresorbable osteogenic scaffolds	Autografts	Allografts
Serious Complications	3	4	4	3	4	3	2
Load bearing function	3	3	2	5	3	4	4
Successful fixation	3	4	2	5	4	4	4
Osseo-integration	3	5	4	2	2	4	4
Availability	2	4	4	5	4	2	4
Tailorability	2	5	2	3	5	3	3
Implant lifespan	2	5	5	2	3	5	4
Duration of intervention	1	2	2	5	2	4	4
TOTAL		78	60	72	65	69	68

5.3. Conclusions

In sum, the advanced strategy for bone defect repair establishes a basis biofabrication platform for subsequent optimization studies, for a parameter-driven mechanistic investigation of the native bone defect repair process, and for the development of a viable, implantable and tailorable product targeting critical size bone defect repair. Indeed, by addressing prior limitations with respect to spatial control, swelling and systemic tailorability, the developed method represents the next step to existing developmental engineering approaches efforts in the realm of bone repair. Moving forward, future work aiming to solidify the platform should include more comprehensive characterization studies validating obtained findings, follow-up cell studies probing both viability and tissue differentiation, and preclinical animal implantation studies assessing repair outcomes.

6. List of references

[1]   M. A. Miranda and M. S. Moon, "Treatment strategy for nonunions and malunions," *Surgical treatment of orthopaedic trauma,* vol. 1, pp. 77-100, 2007.

[2]   C. Court-Brown, S. Rimmer, U. Prakash, and M. McQueen, "The epidemiology of open long bone fractures," *Injury,* vol. 29, pp. 529-534, 1998.

[3]   Z. Gugala, R. W. Lindsey, and S. Gogolewski, "New Approaches in the Treatment of Critical-Size Segmental Defects in Long Bones," in *Macromolecular Symposia*, 2007, pp. 147-161.

[4]   N. M. Haines, W. D. Lack, R. B. Seymour, and M. J. Bosse, "Defining the Lower Limit of a "Critical Bone Defect" in Open Diaphyseal Tibial Fractures," *Journal of orthopaedic trauma,* vol. 30, pp. e158-e163, 2016.

[5]   C. Laurencin, Y. Khan, and S. F. El-Amin, "Bone graft substitutes," *Expert review of medical devices,* vol. 3, pp. 49-57, 2006.

[6]   L. Mirabello, R. J. Troisi, and S. A. Savage, "Osteosarcoma incidence and survival rates from 1973 to 2004," *Cancer,* vol. 115, pp. 1531-1543, 2009.

[7]   D. Gomes, M. Pereira, and A. F. Bettencourt, "Osteomyelitis: an overview of antimicrobial therapy," *Brazilian Journal of Pharmaceutical Sciences,* vol. 49, pp. 13-27, 2013.

[8]   E. Gabrielli, A. Fothergill, L. Brescini, D. Sutton, E. Marchionni, E. Orsetti*, et al.*, "Osteomyelitis caused by Aspergillus species: a review of 310 reported cases," *Clinical Microbiology and Infection,* vol. 20, pp. 559-565, 2014.

[9]   L. Prieto-Pérez, R. Pérez-Tanoira, E. Petkova-Saiz, C. Pérez-Jorge, C. Lopez-Rodriguez, B. Alvarez-Alvarez*, et al.*, "Osteomyelitis: a descriptive study," *Clinics in orthopedic surgery,* vol. 6, pp. 20-25, 2014.

[10]   R. B. Gustilo, R. M. Mendoza, and D. N. Williams, "Problems in the management of type III (severe) open fractures: a new classification of type III open fractures," *Journal of Trauma and Acute Care Surgery,* vol. 24, pp. 742-746, 1984.

[11]   J. Nishida and T. Shimamura, "Methods of reconstruction for bone defect after tumor excision: a review of alternatives," *Medical Science Monitor,* vol. 14, pp. RA107-RA113, 2008.

[12]   E. v. van der Poest Clement, H. Van der Wiel, P. Patka, J. Roos, and P. Lips, "Long-term consequences of fracture of the lower leg: cross-sectional study and long-term longitudinal follow-up of bone mineral density in the hip after fracture of lower leg," *Bone,* vol. 24, pp. 131-134, 1999.

[13]   W. H. Akeson, S. L. Woo, L. Rutherford, R. D. Coutts, M. Gonsalves, and D. Amiel, "The Effects of Rigidity of Internal Fixation Plates on Long Bone Remodeling: A Bio Mechanical and Quantitative Histological Study," *Acta Orthopaedica Scandinavica,* vol. 47, pp. 241-249, 1976.

[14]   E. M. Younger and M. W. Chapman, "Morbidity at bone graft donor sites," *Journal of orthopaedic trauma,* vol. 3, pp. 192-195, 1989.

[15]   K. Søballe, "Hydroxyapatite ceramic coating for bone implant fixation: mechanical and histological studies in dogs," *Acta Orthopaedica Scandinavica,* vol. 64, pp. 1-58, 1993.

[16]   F. Thorey, H. Menzel, C. Lorenz, G. Gross, A. Hoffmann, and H. Windhagen, "Osseointegration by bone morphogenetic protein-2 and transforming growth factor beta2 coated titanium implants in femora of New Zealand white rabbits," *Indian journal of orthopaedics,* vol. 45, p. 57, 2011.

[17]   T. Vo, S. Shah, S. Lu, A. Tatara, E. Lee, T. Roh*, et al.*, "Injectable dual-gelling cell-laden composite hydrogels for bone tissue engineering," *Biomaterials,* vol. 83, pp. 1-11, 2016.

[18]   K. L. Spiller, S. Nassiri, C. E. Witherel, R. R. Anfang, J. Ng, K. R. Nakazawa*, et al.*, "Sequential delivery of immunomodulatory cytokines to facilitate the M1-to-M2 transition of macrophages and enhance vascularization of bone scaffolds," *Biomaterials,* vol. 37, pp. 194-207, 2015.

[19]   P. Yilgor, K. Tuzlakoglu, R. L. Reis, N. Hasirci, and V. Hasirci, "Incorporation of a sequential BMP-2/BMP-7 delivery system into chitosan-based scaffolds for bone tissue engineering," *Biomaterials,* vol. 30, pp. 3551-3559, 2009.

[20]   D. L. Butler, S. A. Goldstein, and F. Guilak, "Functional tissue engineering: the role of biomechanics," *Ann Arbor,* vol. 1001, pp. 77-78, 2000.

[21]   A. R. Amini, C. T. Laurencin, and S. P. Nukavarapu, "Bone tissue engineering: recent advances and challenges," *Critical Reviews™ in Biomedical Engineering,* vol. 40, 2012.

[22]   L. Blecha, P. Zambelli, N. Ramaniraka, P.-E. Bourban, J.-A. Månson, and D. P. Pioletti, "How plate positioning impacts the biomechanics of the open wedge tibial osteotomy; a finite element analysis," *Computer methods in biomechanics and biomedical engineering,* vol. 8, pp. 307-313, 2005.

[23]   D. P. Pioletti, "Biomechanics in bone tissue engineering," *Computer methods in biomechanics and biomedical engineering,* vol. 13, pp. 837-846, 2010.

[24]   S. Bose, M. Roy, and A. Bandyopadhyay, "Recent advances in bone tissue engineering scaffolds," *Trends in biotechnology,* vol. 30, pp. 546-554, 2012.

[25]   S. J. Hollister and W. L. Murphy, "Scaffold translation: barriers between concept and clinic," *Tissue Engineering Part B: Reviews,* vol. 17, pp. 459-474, 2011.

[26]   S. Wade, C. Strader, L. Fitzpatrick, M. Anthony, and C. O'Malley, "Estimating prevalence of osteoporosis: examples from industrialized countries," *Archives of osteoporosis,* vol. 9, pp. 1-10, 2014.

[27]   V. M. Duarte, A. M. Ramos, L. A. Rezende, U. B. Macedo, J. Brandão-Neto, M. G. Almeida*, et al.*, "Osteopenia: a bone disorder associated with diabetes mellitus," *Journal of bone and mineral metabolism,* vol. 23, pp. 58-68, 2005.

[28] S. Egawa, S. Miura, H. Yokoyama, T. Endo, and K. Tamura, "Growth and differentiation of a long bone in limb development, repair and regeneration," *Development, growth & differentiation,* vol. 56, pp. 410-424, 2014.

[29] A. Schindeler, M. M. McDonald, P. Bokko, and D. G. Little, "Bone remodeling during fracture repair: The cellular picture," in *Seminars in cell & developmental biology*, 2008, pp. 459-466.

[30] E. Mackie, Y. Ahmed, L. Tatarczuch, K.-S. Chen, and M. Mirams, "Endochondral ossification: how cartilage is converted into bone in the developing skeleton," *The international journal of biochemistry & cell biology,* vol. 40, pp. 46-62, 2008.

[31] A. White and G. Wallis, "Endochondral ossification: a delicate balance between growth and mineralisation," *Current Biology,* vol. 11, pp. R589-R591, 2001.

[32] B. McKibbin, "The biology of fracture healing in long bones," in *J Bone Joint Surg [Br*, 1978.

[33] F. Freeman, "Chondrogenic and vascular priming: an endochondral ossification approach to bone tissue regeneration," 2015.

[34] E. J. Sheehy, T. Vinardell, C. T. Buckley, and D. J. Kelly, "Engineering osteochondral constructs through spatial regulation of endochondral ossification," *Acta biomaterialia,* vol. 9, pp. 5484-5492, 2013.

[35] C. Scotti, E. Piccinini, H. Takizawa, A. Todorov, P. Bourgine, A. Papadimitropoulos*, et al.*, "Engineering of a functional bone organ through endochondral ossification," *Proceedings of the National Academy of Sciences,* vol. 110, pp. 3997-4002, 2013.

[36] T. Xu, J. M. Miszuk, Y. Zhao, H. Sun, and H. Fong, "Electrospun Polycaprolactone 3D Nanofibrous Scaffold with Interconnected and Hierarchically Structured Pores for Bone Tissue Engineering," *Advanced healthcare materials,* vol. 4, pp. 2238-2246, 2015.

[37]   N. Harada, Y. Watanabe, K. Sato, S. Abe, K. Yamanaka, Y. Sakai*, et al.*, "Bone regeneration in a massive rat femur defect through endochondral ossification achieved with chondrogenically differentiated MSCs in a degradable scaffold," *Biomaterials,* vol. 35, pp. 7800-7810, 2014.

[38]   C. H. Jang, S. H. Ahn, G.-H. Yang, and G. H. Kim, "A MSCs-laden polycaprolactone/collagen scaffold for bone tissue regeneration," *RSC Advances,* vol. 6, pp. 6259-6265, 2016.

[39]   L. D. Loozen, F. Wegman, F. C. Öner, W. J. Dhert, and J. Alblas, "Porous bioprinted constructs in BMP-2 non-viral gene therapy for bone tissue engineering," *Journal of Materials Chemistry B,* vol. 1, pp. 6619-6626, 2013.

[40]   G. Gao, T. Yonezawa, K. Hubbell, G. Dai, and X. Cui, "Inkjet-bioprinted acrylated peptides and PEG hydrogel with human mesenchymal stem cells promote robust bone and cartilage formation with minimal printhead clogging," *Biotechnology journal,* vol. 10, pp. 1568-1577, 2015.

[41]   H.-P. Gerber, T. H. Vu, A. M. Ryan, J. Kowalski, Z. Werb, and N. Ferrara, "VEGF couples hypertrophic cartilage remodeling, ossification and angiogenesis during endochondral bone formation," *Nature medicine,* vol. 5, pp. 623-628, 1999.

[42]   R. Marsell and T. A. Einhorn, "The biology of fracture healing," *Injury,* vol. 42, pp. 551-555, 2011.

[43]   C. T. Brighton and R. M. Hunt, "Early histological and ultrastructural changes in medullary fracture callus," *J Bone Joint Surg Am,* vol. 73, pp. 832-847, 1991.

[44]   C. Mandrycky, Z. Wang, D.-H. Kim, and K. Kim, "3D bioprinting for engineering complex tissues," *Biotechnology Advances,* vol. 34, pp. 422-434, 2016.

[45]   S. V. Murphy and A. Atala, "3D bioprinting of tissues and organs," *Nature biotechnology,* vol. 32, pp. 773-785, 2014.

[46]   I. T. Ozbolat and M. Hospodiuk, "Current advances and future perspectives in extrusion-based bioprinting," *Biomaterials,* vol. 76, pp. 321-343, 2016.

[47]   C. C. Chang, E. D. Boland, S. K. Williams, and J. B. Hoying, "Direct-write bioprinting three-dimensional biohybrid systems for future regenerative therapies," *Journal of Biomedical Materials Research Part B: Applied Biomaterials,* vol. 98, pp. 160-170, 2011.

[48]   T. Boland, V. Mironov, A. Gutowska, E. Roth, and R. R. Markwald, "Cell and organ printing 2: Fusion of cell aggregates in three-dimensional gels," *The Anatomical Record Part A: discoveries in molecular, cellular, and evolutionary biology,* vol. 272, pp. 497-502, 2003.

[49]   A. C. Daly, G. M. Cunniffe, B. N. Sathy, O. Jeon, E. Alsberg, and D. J. Kelly, "3D bioprinting of developmentally inspired templates for whole bone organ engineering," *Advanced healthcare materials,* vol. 5, pp. 2353-2362, 2016.

[50]   S. J. Song, J. Choi, Y. D. Park, J. J. Lee, S. Y. Hong, and K. Sun, "A Three-Dimensional Bioprinting System for Use With a Hydrogel-Based Biomaterial and Printing Parameter Characterization," *Artificial organs,* vol. 34, pp. 1044-1048, 2010.

[51]   S. J. Song, J. Choi, Y. D. Park, S. Hong, J. J. Lee, C. B. Ahn*, et al.*, "Sodium Alginate Hydrogel-Based Bioprinting Using a Novel Multinozzle Bioprinting System," *Artificial organs,* vol. 35, pp. 1132-1136, 2011.

[52]   M. J. Sawkins, P. Mistry, B. N. Brown, K. M. Shakesheff, L. J. Bonassar, and J. Yang, "Cell and protein compatible 3D bioprinting of mechanically strong constructs for bone repair," *Biofabrication,* vol. 7, p. 035004, 2015.

[53]   W. Schuurman, V. Khristov, M. Pot, P. Van Weeren, W. Dhert, and J. Malda, "Bioprinting of hybrid tissue constructs with tailorable mechanical properties," *Biofabrication,* vol. 3, p. 021001, 2011.

[54]   W. Schuurman, P. A. Levett, M. W. Pot, P. R. van Weeren, W. J. Dhert, D. W. Hutmacher*, et al.*, "Gelatin-Methacrylamide Hydrogels as Potential Biomaterials for Fabrication of Tissue-Engineered Cartilage Constructs," *Macromolecular bioscience,* vol. 13, pp. 551-561, 2013.

[55]   T. Zhang, K. C. Yan, L. Ouyang, and W. Sun, "Mechanical characterization of bioprinted in vitro
        soft tissue models," *Biofabrication,* vol. 5, p. 045010, 2013.

[56]   F. Ganji, S. Vasheghani-Farahani, and E. Vasheghani-Farahani, "Theoretical description of
        hydrogel swelling: a review," *Iran Polym J,* vol. 19, pp. 375-398, 2010.

[57]   G. Evmenenko and T. Budtova, "Structural changes in hydrogels immersed in a linear polymer
        solution, studied by SANS," *Polymer,* vol. 41, pp. 4943-4947, 2000.

[58]   A. A. Lloyd, Z. X. Wang, and E. Donnelly, "Multiscale contribution of bone tissue material
        property heterogeneity to trabecular bone mechanical behavior," *Journal of biomechanical
        engineering,* vol. 137, p. 010801, 2015.

[59]   M. Stauber and R. Müller, "Volumetric spatial decomposition of trabecular bone into rods and
        plates—a new method for local bone morphometry," *Bone,* vol. 38, pp. 475-484, 2006.

[60]   X. S. Liu, P. Sajda, P. K. Saha, F. W. Wehrli, G. Bevill, T. M. Keaveny*, et al.*, "Complete volumetric
        decomposition of individual trabecular plates and rods and its morphological correlations with
        anisotropic elastic moduli in human trabecular bone," *Journal of Bone and Mineral Research,*
        vol. 23, pp. 223-235, 2008.

[61]   Y. N. Yeni, M. J. Zinno, J. S. Yerramshetty, R. Zauel, and D. P. Fyhrie, "Variability of trabecular
        microstructure is age-, gender-, race-and anatomic site-dependent and affects stiffness and
        stress distribution properties of human vertebral cancellous bone," *Bone,* vol. 49, pp. 886-894,
        2011.

[62]   G. A. Sathi, K. Kenmizaki, S. Yamaguchi, H. Nagatsuka, Y. Yoshida, A. Matsugaki*, et al.*, "Early
        initiation of endochondral ossification of mouse femur cultured in hydrogel with different
        mechanical stiffness," *Tissue Engineering Part C: Methods,* vol. 21, pp. 567-575, 2015.

[63]   D. R. Carter and M. Wong, "Mechanical stresses and endochondral ossification in the
        chondroepiphysis," *Journal of orthopaedic research,* vol. 6, pp. 148-154, 1988.

[64]   B. Ji, W. Jiang, Z. Tang, C. Liang, Y. Zhang, and H. Wang, "Finite Element Analysis of the Effect of Mastication on Endochondral Ossification During the Consolidation Period of Mandibular Distraction Osteogenesis," *Arabian Journal for Science and Engineering,* vol. 39, pp. 7223-7228, 2014.

[65]   S. Ray, U. Thormann, U. Sommer, T. El Khassawna, M. Hundgeburth, A. Henß*, et al.*, "Effects of macroporous, strontium loaded xerogel-scaffolds on new bone formation in critical-size metaphyseal fracture defects in ovariectomized rats," *Injury,* vol. 47, pp. S52-S61, 2016.

[66]   L. Polo-Corrales, M. Latorre-Esteves, and J. E. Ramirez-Vick, "Scaffold design for bone regeneration," *Journal of nanoscience and nanotechnology,* vol. 14, pp. 15-56, 2014.

[67]   L. V. Bossche and G. Vanderstraeten, "Heterotopic ossification: a review," *J Rehabil Med,* vol. 37, pp. 129-36, 2005.

[68]   L. Vikingsson, B. Claessens, J. Gómez-Tejedor, G. G. Ferrer, and J. G. Ribelles, "Relationship between micro-porosity, water permeability and mechanical behavior in scaffolds for cartilage engineering," *Journal of the mechanical behavior of biomedical materials,* vol. 48, pp. 60-69, 2015.

[69]   M. Laasanen, J. Töyräs, R. Korhonen, J. Rieppo, S. Saarakkala, M. Nieminen*, et al.*, "Biomechanical properties of knee articular cartilage," *Biorheology,* vol. 40, pp. 133-140, 2003.

[70]   B. Li, Y.-P. Cao, X.-Q. Feng, and H. Gao, "Mechanics of morphological instabilities and surface wrinkling in soft materials: a review," *Soft Matter,* vol. 8, pp. 5728-5745, 2012.

[71]   D. Eglin, D. Mortisen, and M. Alini, "Degradation of synthetic polymeric scaffolds for bone and cartilage tissue repairs," *Soft Matter,* vol. 5, pp. 938-947, 2009.

[72]   V. Karageorgiou and D. Kaplan, "Porosity of 3D biomaterial scaffolds and osteogenesis," *Biomaterials,* vol. 26, pp. 5474-5491, 2005.

[73]   S. Teixeira, M. Rodriguez, P. Pena, A. De Aza, S. De Aza, M. Ferraz*, et al.*, "Physical characterization of hydroxyapatite porous scaffolds for tissue engineering," *Materials Science and Engineering: C,* vol. 29, pp. 1510-1514, 2009.

[74]   C. Bony, M. Cren, S. Domergue, K. Toupet, C. Jorgensen, and D. Noël, "adipose Mesenchymal stem cells isolated after Manual or Water-jet-assisted liposuction Display similar Properties," *Frontiers in immunology,* vol. 6, 2015.

[75]   J. W. Nichol, S. T. Koshy, H. Bae, C. M. Hwang, S. Yamanlar, and A. Khademhosseini, "Cell-laden microengineered gelatin methacrylate hydrogels," *Biomaterials,* vol. 31, pp. 5536-5544, 2010.

[76]   D. B. Kolesky, R. L. Truby, A. Gladman, T. A. Busbee, K. A. Homan, and J. A. Lewis, "3D Bioprinting of Vascularized, Heterogeneous Cell-Laden Tissue Constructs," *Advanced Materials,* vol. 26, pp. 3124-3130, 2014.

[77]   H. Shin, B. D. Olsen, and A. Khademhosseini, "The mechanical properties and cytotoxicity of cell-laden double-network hydrogels based on photocrosslinkable gelatin and gellan gum biomacromolecules," *Biomaterials,* vol. 33, pp. 3143-3152, 2012.

[78]   T. Billiet, E. Gevaert, T. De Schryver, M. Cornelissen, and P. Dubruel, "The 3D printing of gelatin methacrylamide cell-laden tissue-engineered constructs with high cell viability," *Biomaterials,* vol. 35, pp. 49-62, 2014.

[79]   K. Liu and T. C. Ovaert, "Poro-viscoelastic constitutive modeling of unconfined creep of hydrogels using finite element analysis with integrated optimization method," *Journal of the mechanical behavior of biomedical materials,* vol. 4, pp. 440-450, 2011.

[80]   P. Silva, S. Crozier, M. Veidt, and M. J. Pearcy, "An experimental and finite element poroelastic creep response analysis of an intervertebral hydrogel disc model in axial compression," *Journal of Materials Science: Materials in Medicine,* vol. 16, pp. 663-669, 2005.

[81]   M. Oyen, "Mechanical characterisation of hydrogel materials," *International Materials Reviews,* vol. 59, pp. 44-59, 2014.

[82]   B. D. Fairbanks, M. P. Schwartz, C. N. Bowman, and K. S. Anseth, "Photoinitiated polymerization of PEG-diacrylate with lithium phenyl-2, 4, 6-trimethylbenzoylphosphinate: polymerization rate and cytocompatibility," *Biomaterials,* vol. 30, pp. 6702-6707, 2009.

[83]   H. Lin, D. Zhang, P. G. Alexander, G. Yang, J. Tan, A. W.-M. Cheng*, et al.*, "Application of visible light-based projection stereolithography for live cell-scaffold fabrication with designed architecture," *Biomaterials,* vol. 34, pp. 331-339, 2013.

[84]   S. Preibisch, S. Saalfeld, and P. Tomancak, "Globally optimal stitching of tiled 3D microscopic image acquisitions," *Bioinformatics,* vol. 25, pp. 1463-1465, 2009.

[85]   S. Benedikt, J. Wang, M. Markovic, N. Moszner, K. Dietliker, A. Ovsianikov*, et al.*, "Highly efficient water-soluble visible light photoinitiators," *Journal of Polymer Science Part A: Polymer Chemistry,* vol. 54, pp. 473-479, 2016.

[86]   S. R. Sternberg, "Biomedical image processing," *Computer,* vol. 16, pp. 22-34, 1983.

[87]   K. L. Spiller, S. J. Laurencin, D. Charlton, S. A. Maher, and A. M. Lowman, "Superporous hydrogels for cartilage repair: Evaluation of the morphological and mechanical properties," *Acta biomaterialia,* vol. 4, pp. 17-25, 2008.

[88]   M. Domingos, F. Chiellini, A. Gloria, L. Ambrosio, P. Bartolo, and E. Chiellini, "Effect of process parameters on the morphological and mechanical properties of 3D bioextruded poly (ϵ-caprolactone) scaffolds," *Rapid Prototyping Journal,* vol. 18, pp. 56-67, 2012.

[89]   K. Iwami and N. Umeda, *Rapid Prototyping in Biomedical Engineering*: INTECH Open Access Publisher, 2011.

[90]   N. E. Fedorovich, W. Schuurman, H. M. Wijnberg, H.-J. Prins, P. R. van Weeren, J. Malda*, et al.*, "Biofabrication of osteochondral tissue equivalents by printing topologically defined, cell-laden hydrogel scaffolds," *Tissue Engineering Part C: Methods,* vol. 18, pp. 33-44, 2011.

[91]   B. A. Aguado, W. Mulyasasmita, J. Su, K. J. Lampe, and S. C. Heilshorn, "Improving viability of stem cells during syringe needle flow through the design of hydrogel cell carriers," *Tissue Engineering Part A,* vol. 18, pp. 806-815, 2011.

[92]   A. M. Yousefi, C. Gauvin, L. Sun, R. W. DiRaddo, and J. Fernandes, "Design and fabrication of 3D-plotted polymeric scaffolds in functional tissue engineering," *Polymer Engineering & Science,* vol. 47, pp. 608-618, 2007.

[93]   R. El-Ayoubi, C. DeGrandpré, R. DiRaddo, P. Lavigne, and A.-M. Yousefi, "Design and Dynamic Culture of 3D Scaffolds for Cartilage Tissue Engineering," *Journal of biomaterials applications,* 2009.

[94]   X. Cui, K. Breitenkamp, M. Finn, M. Lotz, and D. D. D'Lima, "Direct human cartilage repair using three-dimensional bioprinting technology," *Tissue Engineering Part A,* vol. 18, pp. 1304-1312, 2012.

[95]   R. E. Saunders and B. Derby, "Inkjet printing biomaterials for tissue engineering: bioprinting," *International Materials Reviews,* vol. 59, pp. 430-448, 2014.

[96]   J. Glowacki and S. Mizuno, "Collagen scaffolds for tissue engineering," *Biopolymers,* vol. 89, pp. 338-344, 2008.

[97]   M. N. Collins and C. Birkinshaw, "Hyaluronic acid based scaffolds for tissue engineering—A review," *Carbohydrate polymers,* vol. 92, pp. 1262-1279, 2013.

[98]   J. Sun and H. Tan, "Alginate-based biomaterials for regenerative medicine applications," *Materials,* vol. 6, pp. 1285-1309, 2013.

[99] M. L. Oyen, "Nanoindentation of hydrated materials and tissues," *Current Opinion in Solid State and Materials Science,* vol. 19, pp. 317-323, 2015.

[100] K. L. Spiller, S. J. Laurencin, and A. M. Lowman, "Characterization of the behavior of porous hydrogels in model osmotically-conditioned articular cartilage systems," *Journal of Biomedical Materials Research Part B: Applied Biomaterials,* vol. 90, pp. 752-759, 2009.

[101] L. J. Melton, "Epidemiology of Fractures-Chapter 1," 1995.

[102] S. Kontulainen, J. Johnston, D. Liu, C. Leung, T. Oxland, and H. McKay, "Strength indices from pQCT imaging predict up to 85% of variance in bone failure properties at tibial epiphysis and diaphysis," *J Musculoskelet Neuronal Interact,* vol. 8, pp. 401-9, 2008.

[103] D. C. Mann and S. Rajmaira, "Distribution of physeal and nonphyseal fractures in 2,650 long-bone fractures in children aged 0-16 years," *Journal of Pediatric Orthopaedics,* vol. 10, pp. 713-716, 1990.

[104] D. Smrke, P. Rozman, and B. G. MatjazVeselko, "Treatment of Bone Defects-Allogenic Platelet Gel and Autologous Bone Technique," *Regenerative Medicine and Tissue Engineering, Prof. Jose A. Andrades (Ed.), InTech,* 2013.

[105] S.-H. Chen, M. Lei, X.-H. Xie, L.-Z. Zheng, D. Yao, X.-L. Wang*, et al.*, "PLGA/TCP composite scaffold incorporating bioactive phytomolecule icaritin for enhancement of bone defect repair in rabbits," *Acta biomaterialia,* vol. 9, pp. 6711-6722, 2013.

[106] S. Berahmani, D. Janssen, S. van Kessel, D. Wolfson, M. de Waal Malefijt, P. Buma*, et al.*, "An experimental study to investigate biomechanical aspects of the initial stability of press-fit implants," *Journal of the mechanical behavior of biomedical materials,* vol. 42, pp. 177-185, 2015.

[107] J. R. Field, H. Törnkvist, T. C. Hearn, G. Sumner-Smith, and T. D. Woodside, "The influence of screw omission on construction stiffness and bone surface strain in the application of bone plates to cadaveric bone," *Injury,* vol. 30, pp. 591-598, 1999.

[108] R. M. A. R. Izaham, M. R. A. Kadir, A. H. A. Rashid, M. G. Hossain, and T. Kamarul, "Finite element analysis of Puddu and Tomofix plate fixation for open wedge high tibial osteotomy," *Injury,* vol. 43, pp. 898-902, 2012.

[109] O. Franke, K. Durst, V. Maier, M. Göken, T. Birkholz, H. Schneider*, et al.*, "Mechanical properties of hyaline and repair cartilage studied by nanoindentation," *Acta Biomaterialia,* vol. 3, pp. 873-881, 2007.

[110] P. Leong and E. Morgan, "Measurement of fracture callus material properties via nanoindentation," *Acta biomaterialia,* vol. 4, pp. 1569-1575, 2008.

[111] S. J. Shefelbine, U. Simon, L. Claes, A. Gold, Y. Gabet, I. Bab*, et al.*, "Prediction of fracture callus mechanical properties using micro-CT images and voxel-based finite element analysis," *Bone,* vol. 36, pp. 480-488, 2005.

[112] P. L. Leong and E. F. Morgan, "Correlations between indentation modulus and mineral density in bone-fracture calluses," *Integrative and comparative biology,* vol. 49, pp. 59-68, 2009.

[113] J. Yi, R. F. LeBouf, M. G. Duling, T. Nurkiewicz, B. T. Chen, D. Schwegler-Berry*, et al.*, "Emission of particulate matter from a desktop three-dimensional (3D) printer," *Journal of Toxicology and Environmental Health, Part A,* vol. 79, pp. 453-465, 2016.

[114] G. Renders, L. Mulder, L. Van Ruijven, and T. Van Eijden, "Porosity of human mandibular condylar bone," *Journal of anatomy,* vol. 210, pp. 239-248, 2007.

[115] D. R. Carter and W. C. Hayes, "The compressive behavior of bone as a two-phase porous structure," *The Journal of Bone & Joint Surgery,* vol. 59, pp. 954-962, 1977.

[116] J. Kim, I. S. Kim, T. H. Cho, K. B. Lee, S. J. Hwang, G. Tae*, et al.*, "Bone regeneration using hyaluronic acid-based hydrogel with bone morphogenic protein-2 and human mesenchymal stem cells," *Biomaterials,* vol. 28, pp. 1830-1837, 2007.

[117] R. Vecchione, G. Pitingolo, A. P. Falanga, D. Guarnieri, and P. A. Netti, "Confined Gelatin Dehydration as a Viable Route To Go Beyond Micromilling Resolution and Miniaturize Biological Assays," *ACS applied materials & interfaces,* vol. 8, pp. 12075-12081, 2016.

[118] B. S. Kim, J. Jang, S. Chae, G. Gao, J.-S. Kong, M. Ahn*, et al.*, "Three-dimensional bioprinting of cell-laden constructs with polycaprolactone protective layers for using various thermoplastic polymers," *Biofabrication,* vol. 8, p. 035013, 2016.

[119] J. M. Harris, *Poly (ethylene glycol) chemistry: biotechnical and biomedical applications*: Springer Science & Business Media, 2013.

[120] J. T. Oliveira, L. Martins, R. Picciochi, P. Malafaya, R. Sousa, N. Neves*, et al.*, "Gellan gum: a new biomaterial for cartilage tissue engineering applications," *Journal of biomedical materials research Part A,* vol. 93, pp. 852-863, 2010.

[121] K. Y. Lee, J. Shim, and H. G. Lee, "Mechanical properties of gellan and gelatin composite films," *Carbohydrate Polymers,* vol. 56, pp. 251-254, 2004.

[122] K. Nair, M. Gandhi, S. Khalil, K. C. Yan, M. Marcolongo, K. Barbee*, et al.*, "Characterization of cell viability during bioprinting processes," *Biotechnology journal,* vol. 4, pp. 1168-1177, 2009.

[123] S. Eshraghi and S. Das, "Mechanical and microstructural properties of polycaprolactone scaffolds with one-dimensional, two-dimensional, and three-dimensional orthogonally oriented porous architectures produced by selective laser sintering," *Acta Biomater,* vol. 6, pp. 2467-76, Jul 2010.

[124] C. Chen, Y. Shi, Y. Zhang, J. Zhu, and Y. Yan, "Size dependence of Young's modulus in ZnO nanowires," *Physical review letters,* vol. 96, p. 075505, 2006.

[125] L. Sun, R. P. Han, J. Wang, and C. Lim, "Modeling the size-dependent elastic properties of polymeric nanofibers," *Nanotechnology,* vol. 19, p. 455706, 2008.

[126] J. A. Stammen, S. Williams, D. N. Ku, and R. E. Guldberg, "Mechanical properties of a novel PVA hydrogel in shear and unconfined compression," *Biomaterials,* vol. 22, pp. 799-806, 2001.

[127] S. Reitmaier, U. Wolfram, A. Ignatius, H.-J. Wilke, A. Gloria, J. M. Martín-Martínez*, et al.*, "Hydrogels for nucleus replacement—facing the biomechanical challenge," *journal of the mechanical behavior of biomedical materials,* vol. 14, pp. 67-77, 2012.

[128] S. Munir, C. B. Foldager, M. Lind, V. Zachar, K. Søballe, and T. G. Koch, "Hypoxia enhances chondrogenic differentiation of human adipose tissue-derived stromal cells in scaffold-free and scaffold systems," *Cell and tissue research,* vol. 355, pp. 89-102, 2014.

[129] V. V. Meretoja, R. L. Dahlin, S. Wright, F. K. Kasper, and A. G. Mikos, "The effect of hypoxia on the chondrogenic differentiation of co-cultured articular chondrocytes and mesenchymal stem cells in scaffolds," *Biomaterials,* vol. 34, pp. 4266-4273, 2013.